GNSS Multipath-Resistant Cooperative Navigation in Urban Vehicular Networks

Hyunwoo Ko, Binhee Kim, *Student Member, IEEE*, and Seung-Hyun Kong, *Member, IEEE*

***Abstract*—Multipath delays and signal outages in urban environments have been the most difficult problems in Global Navigation Satellite System (GNSS)-based cooperative vehicular navigation systems. In this paper, we develop a non-line-of-sight (NLOS) GNSS signal detection algorithm and propose a multipath-resistant hybrid sum–product algorithm over a wireless network (MRH-SPAWN) and multipath-resistant hybrid cooperative extended Kalman filter (MR-hcEKF) techniques that significantly enhance multipath robustness in urban environments, compared with H-SPAWN and hcEKF, respectively. We provide theoretical derivation and realization of the proposed techniques and demonstrate the performance with numerous Monte Carlo simulations using field measurements of multipath delays. The proposed techniques significantly improve the positioning accuracy of all vehicles and outperform the conventional cooperative positioning (CP) technique in urban multipath environments.**

***Index Terms*—Cooperative positioning (CP), hybrid sum–product algorithm over wireless network (H-SPAWN), hybrid cooperative extended-KF (hcEKF), multipath mitigation, vehicular network.**

I. Introduction

VEHICULAR navigation technologies have become a vital component in most transportation systems as they provide convenience, location-related information, and safety to transportation users [1]. In addition, recent vehicular navigation technologies for transportation systems require the precise positioning of the user vehicle and neighboring vehicles to improve performance and safety.

Among the component technologies of vehicular navigation systems, the Global Navigation Satellite System (GNSS) provides absolute and precise positions of vehicles. It has therefore been the core enabler of vehicular navigation systems and services. However, GNSS is also associated with various errors, such as those arising from satellite clocks, ephemeris errors, and ionosphere and troposphere delays [2], resulting in more than 10 m of positioning error in practice. In urban environments, GNSS non-line-of-sight (NLOS) (i.e., multipath) delays and local signal outages due to shadowing behind buildings can cause positioning errors as large as a few hundred meters [3]. While it has been found that differential GNSS (DGNSS) can correct some of the errors in GNSS pseudorange measurements and provide meter-level positioning accuracy in open-sky LOS environments, DGNSS cannot compensate for NLOS delays and signal outages in urban environments.

To solve the issues of NLOS delays and the signal outages, there have been a number of techniques introduced in the literature. Among them, the sensor fusion technique, which combines the GNSS, inertial navigation system (INS), and odometer [4] has been a common technique for vehicular navigation systems. However, because INS and odometer errors diverge rapidly over time, sensor fusion techniques may not be able to maintain acceptable navigation performance for long GNSS signal outages or in the event of considerable NLOS delays.

Given that many vehicles are expected to be connected in the near future [5], cooperative positioning (CP) techniques utilizing local measurements between wireless nodes [6] (i.e., vehicles) have become useful in the field of cooperative vehicular navigation. In the majority of CP techniques, wireless nodes measure local ranges relative to their peer nodes (i.e., neighboring vehicles) using radio signals such as ultra-wideband (UWB) [7] signals; the systems cooperatively exchange their own position estimates for further improvements of their position estimate accuracy. There are CP techniques that utilize local measurements other than ranging: In one study [8], the Doppler shift of radio signals is used to improve robustness against channel fading and multipath environments, whereas another study utilizes the pseudorange double difference [9].

Kalman filter (KF)-based algorithms such as the extended KF (EKF) [8]–[11] and the unscented KF [10] algorithms are generally used for data fusion. Specifically, the EKF is widely used, as it is easy to implement and achieves good position estimation performance. The hybrid cooperative EKF (hcEKF) [10] technique that additionally utilizes radio ranging measurements is one of the most recent EKF-based CP technique and offers the lowest computational cost. In general, the CP technique, based on a particle filter [12], outperforms KF-based techniques in terms of position estimation accuracy; however, it is computationally expensive. In the sum–product algorithm over wireless network (SPAWN) [13], data-fusion-based state estimation is modeled by a state estimation problem in a Bayesian network. It is found that belief propagation (BP) [14], a sum–product message-passing algorithm used in Bayesian networks, achieves near-optimal state estimation performance (superior to EKF) with a low computational cost. The hybrid SPAWN [15] (H-SPAWN) algorithm, which integrates GNSS

Manuscript received April 1, 2015; revised July 15, 2015 and September 1, 2015; accepted September 21, 2015. Date of publication September 23, 2015; date of current version December 14, 2015. This work was supported by the Mid-career Research Program through an NRF grant funded by the Korean government (MEST) under Grant 2013R1A2A2A01067863. The review of this paper was coordinated by the Guest Editors. *(Corresponding author: Seung-Hyun Kong.)*

The authors are with the Cho Chun Shik Graduate School for Green Transportation, Korea Advanced Institute of Science and Technology, Daejeon 305 701, Korea (e-mail: kohyunwoo@kaist.ac.kr; vini@kaist.ac.kr; skong@kaist.ac.kr).

Color versions of one or more of the figures in this paper are available online at http://ieeexplore.ieee.org.

Digital Object Identifier 10.1109/TVT.2015.2481509

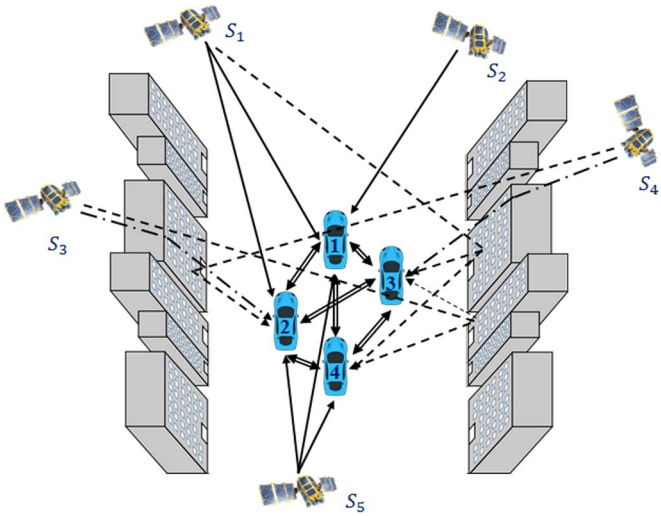

Fig. 1. GNSS signals and cooperative vehicular network in urban environments.

measurements with the SPAWN [13], significantly increases positioning availability during local GNSS outages, thus improving the overall positioning accuracy of connected vehicles.

However, hcEKF, H-SPAWN, and other CP techniques using GNSS are vulnerable to NLOS delays in urban environments and can produce large positioning errors. Fig. 1 shows an example of connected vehicles using GNSS in an urban environment. Neighboring vehicles measure local ranges relative to each other, as shown by the double-lined arrows, and then obtain pseudoranges from a different set of satellites. A satellite signal can be a LOS to vehicles as indicated by the solid arrows and can be an NLOS to other vehicles, as shown by the dashed arrows and dash-dot arrows, which represent reflected signals and diffracted signals, respectively.

GNSS multipath mitigation techniques have been studied in various ways; GNSS receivers can use computationally expensive signal processing techniques, such as the least-squares iterative multipath super-resolution (LIMS) [16]. They can also utilize expensive additional receiver hardware such as multi-antenna configurations [17] and cameras [18] or statistical algorithms such as the receiver autonomous integrity monitoring (RAIM) technique [19]. However, RAIM techniques based on statistical testing [20] increase the computational complexity of the receiver and may produce inaccurate solutions in multipath environments, depending on the number of NLOS satellites and LOS satellites [21].

In this paper, we propose a multipath-resistant (MR) NLOS detection algorithm (ND algorithm) for CP techniques that uses GNSS. We implement the proposed algorithm into H-SPAWN and hcEKF and propose MRH-SPAWN and MR-hcEKF techniques for CP since H-SPAWN is a high-performance CP technique and hcEKF is a computationally efficient CP technique, and both H-SPAWN and hcEKF use GNSS and local ranging. The proposed ND algorithm utilizes relatively accurate local range measurements between vehicles and pseudorange measurements to compile a statistics for the LOS signals, after which it compares the statistics to those of the other GNSS pseudorange measurements. The proposed ND algorithm can build useful statistics of LOS signals with only local range measurements and successfully detects GNSS pseudoranges corrupted by NLOS delays. In addition, the performance of the proposed ND algorithm does not depend on the numbers of NLOS or LOS satellites. The proposed MRH-SPAWN technique implements the proposed algorithm into H-SPAWN with additional factor graphs, and MR-hcEKF implements the proposed algorithm into hcEKF as an external algorithm. The proposed techniques, i.e., MRH-SPAWN and MR-hcEKF, outperform H-SPAWN and hcEKF and demonstrate significant positioning improvements in GNSS multipath environments.

The remainder of this paper is organized as follows. In Section II, we introduce the system model and notations used in this paper. In Section III, we propose the ND algorithm, and the proposed techniques, i.e., MRH-SPAWN and MR-hcEKF, are described in Section IV. We provide the results of numerous Monte Carlo simulations using NLOS delay measurements observed in real urban environments to demonstrate the superior performance of the proposed techniques relative to the conventional techniques, i.e., H-SPAWN and EKF, in Section V, and conclude this paper in Section VI.

Throughout this paper, the following conventions are used for notations. Vectors or matrices are denoted by boldface symbols. Lowercase letters are used for scalars and vectors, and capital letters are used for matrices.

II. System Model

Here, we introduce the general system model considered in this paper and define notations with geometric relationships. We also describe some of the assumptions made with regard to the proposed techniques (i.e., MRH-SPAWN and MR-hcEKF).

Consider a set of nodes U, whose elements can communicate with each other in urban environments, and the user (node) $u \in U$. The m-th node $n_m \in U$ $(m \in [1, 2, \ldots, M])$ receives GNSS signals from a subset of satellites S_m of all detectable satellites S. The set of peer nodes around user u at the k-th time instant t_k is denoted $U_u^{(k)}$, and the set of satellites whose pseudoranges are measured by user u at t_k is denoted $S_u^{(k)}$. The position state vector $\mathbf{P}_i^{(k)} = [x_i^{(k)} y_i^{(k)} z_i^{(k)}]^T$ is used to express the positions of the satellites, the peer nodes, and the user, when $i = s$, $i = n$, and $i = u$, respectively. The receiver clock bias of user u is denoted in time as $\delta^{(k)}$, and can be expressed in distance as $b^{(k)} = c \cdot \delta^{(k)}$, where c is the speed of light. The respective true state, predicted (i.e., *a priori*) state, and estimated (i.e., *a posteriori*) state of the user u are defined as follows:

$$\mathbf{x}_u^{(k)} = \left[\mathbf{P}_u^{(k)^T} \;\; b^{(k)}\right]^T \tag{1a}$$

$$\hat{\mathbf{x}}_u^{-(k)} = \left[\hat{\mathbf{P}}_u^{-(k)^T} \;\; \hat{b}^{-(k)}\right]^T \tag{1b}$$

$$\hat{\mathbf{x}}_u^{(k)} = \left[\hat{\mathbf{P}}_u^{(k)^T} \;\; \hat{b}^{(k)}\right]^T. \tag{1c}$$

Fig. 2 provides an example of urban vehicular environments, in which a satellite, the user, and a peer node are located at $\mathbf{P}_s^{(k)}$, $\mathbf{P}_u^{(k)}$, and $\mathbf{P}_n^{(k)}$, respectively, and in which vehicles are

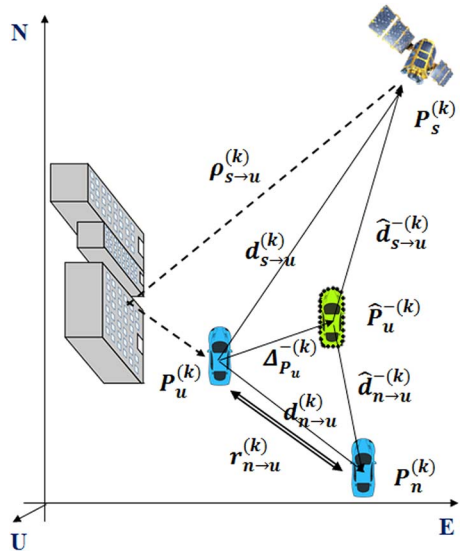

Fig. 2. Example of the urban vehicle environment.

considered nodes. The predicted position of the user $\hat{\mathbf{P}}_u^{-(k)}$ is depicted by a node whose boundary is drawn with a dotted line. We assume that we have sufficient knowledge of the node's dynamics and that the time interval $\Delta t = t_k - t_{k-1}$ between the position estimates is small enough so that the predicted position has a small degree of error. However, in practice, the estimated position $\hat{\mathbf{P}}_u^{(k)}$ may have a large error in the presence of NLOS delays, as denoted by τ in distance. We do not show the estimated position in Fig. 2, but it can be any position from $\mathbf{P}_u^{(k)}$ within a radius $\Delta_{\mathbf{P}_{\max}}$, which can be a few hundred meters [3]. The predicted and estimated position errors (i.e., *a priori* and *a posteriori* errors, respectively) are expressed as

$$\Delta_{\mathbf{P}_u}^{-(k)} = \mathbf{P}_u^{(k)} - \hat{\mathbf{P}}_u^{-(k)} \tag{2a}$$

$$\Delta_{\mathbf{P}_u}^{(k)} = \mathbf{P}_u^{(k)} - \hat{\mathbf{P}}_u^{(k)} \tag{2b}$$

respectively. The true range between the satellite s and user u, the predicted pseudorange between s and $\hat{\mathbf{P}}_u^{-(k)}$, and the estimated pseudorange between s and $\hat{\mathbf{P}}_u^{(k)}$ are defined as

$$d_{s\to u}^{(k)} = \left\| \mathbf{P}_s^{(k)} - \mathbf{P}_u^{(k)} \right\|_2 \tag{3a}$$

$$\hat{d}_{s\to u}^{-(k)} = \left\| \mathbf{P}_s^{(k)} - \hat{\mathbf{P}}_u^{-(k)} \right\|_2 \tag{3b}$$

$$\hat{d}_{s\to u}^{(k)} = \left\| \mathbf{P}_s^{(k)} - \hat{\mathbf{P}}_u^{(k)} \right\|_2 \tag{3c}$$

respectively. In Fig. 2, the measured pseudorange $\rho_{s\to u}^{(k)}$ is corrupted by an NLOS delay, and $\rho_{s\to u}^{(k)}$ can be expressed in terms of the true range, user clock bias, noise error, and NLOS delay as follows:

$$\rho_{s\to u}^{(k)} = d_{s\to u}^{(k)} + b^{(k)} + v_{s\to u}^{(k)} + \tau^{(k)} \tag{4}$$

where the clock bias is from inaccurate position estimate at the previous time step and where $v_{s\to u}^{(k)}$ represents the pseudorange (measurement) noise error.

Similarly, the true local range between node n and user u, the predicted local range between n and $\hat{\mathbf{P}}_u^{-(k)}$, and the estimated local range between n and $\hat{\mathbf{P}}_u^{(k)}$ are expressed as

$$d_{n\to u}^{(k)} = \left\| \mathbf{P}_n^{(k)} - \mathbf{P}_u^{(k)} \right\|_2 \tag{5a}$$

$$\hat{d}_{n\to u}^{-(k)} = \left\| \mathbf{P}_n^{(k)} - \hat{\mathbf{P}}_u^{-(k)} \right\|_2 \tag{5b}$$

$$\hat{d}_{n\to u}^{(k)} = \left\| \mathbf{P}_n^{(k)} - \hat{\mathbf{P}}_u^{(k)} \right\|_2 \tag{5c}$$

respectively, and using the true local range and local range (measurement) noise error $v_{n\to u}^{(k)}$, the measured local range can be expressed as follows:

$$r_{n\to u}^{(k)} = d_{n\to u}^{(k)} + v_{n\to u}^{(k)} \tag{6}$$

where $v_{n\to u}^{(k)}$ is assumed very small (< 1 m) for ranging techniques such as UWB two-way ranging [7]. In Fig. 2, the measured local range is shown with a double-lined arrow. Note that a measured local range may be corrupted by an NLOS delay; however, because UWB has a high temporal resolution [7], multipath effects in UWB are neglected in this paper.

To improve the positioning accuracy, the measured pseudoranges corrupted by NLOS delays should be detected and deweighted appropriately in the final position fix. For the ND algorithm proposed in Section III, the measured pseudorange $\rho_{s\to u}^{(k)}$ and the measured local range $r_{n\to u}^{(k)}$ should be expressed in terms of the predicted pseudorange $\hat{d}_{s\to u}^{-(k)}$ and the predicted local range $\hat{d}_{n\to u}^{-(k)}$, respectively, with their residuals. Given that the predicted position $\hat{\mathbf{P}}_u^{-(k)}$ has much smaller error than that of the NLOS delay $\tau^{(k)}$, the true range $d_{s\to u}^{(k)}$ can be linearized around the predicted position $\hat{\mathbf{P}}_u^{-(k)}$ using the Taylor series and expressed in terms of $\hat{d}_{s\to u}^{-(k)}$ and a small residual term as follows:

$$\begin{aligned} d_{s\to u}^{(k)} &= \sqrt{\left(x_u^{(k)} - x_s^{(k)}\right)^2 + \left(y_u^{(k)} - y_s^{(k)}\right)^2 + \left(z_u^{(k)} - z_s^{(k)}\right)^2}\Bigg|_{\hat{\mathbf{P}}_u^{-(k)}} \\ &\simeq \hat{d}_{s\to u}^{-(k)} + \Delta_{\mathbf{P}_u}^{-(k)T} \left(\frac{\hat{\mathbf{P}}_u^{-(k)} - \mathbf{P}_s^{(k)}}{d_{s\to u}^{(k)}} \right) \\ &\simeq \hat{d}_{s\to u}^{-(k)} + \Delta_{\mathbf{P}_u}^{-(k)T} \mathbf{g}_s^{(k)} \end{aligned} \tag{7}$$

where the satellite direction vector $\mathbf{g}_s^{(k)} \simeq (\hat{\mathbf{P}}_u^{-(k)} - \mathbf{P}_s^{(k)})/\hat{d}_{s\to u}^{-(k)}$ is obtained with an approximation $d_{s\to u}^{(k)} \simeq \hat{d}_{s\to u}^{-(k)}$. Denoting $\rho_{s_l\to u}^{(k)}$ and $d_{s_l\to u}^{(k)}$ as the measured pseudorange and the true range of the l-th satellite ($l \in \{1, 2, \ldots, L\}$), respectively, the set of L measured pseudoranges can be expressed as

$$\boldsymbol{\rho}_s^{(k)} \simeq \hat{\mathbf{d}}_s^{(k)} + \mathbf{G}_s^{(k)} \Delta_{\mathbf{P}_u}^{-(k)} + \mathbf{b}^{(k)} + \mathbf{v}_s^{(k)} + \boldsymbol{\tau}^{(k)} \tag{8}$$

where the l-th elements of $\boldsymbol{\rho}_s^{(k)}$, $\hat{\mathbf{d}}_s^{(k)}$, $\mathbf{v}_s^{(k)}$, and $\boldsymbol{\tau}^{(k)}$ are $\rho_{s_l\to u}^{(k)}$, $\hat{d}_{s_l\to u}^{-(k)}$, $v_{s_l\to u}^{(k)}$, and $\tau_l^{(k)}$, respectively; the l-th row of $\mathbf{G}_s^{(k)}$ is the direction to the l-th satellite $\mathbf{g}_{s_l}^{(k)}$, and $\mathbf{b}^{(k)} = [b^{(k)}, b^{(k)}, \ldots, b^{(k)}]^T$ is a $[L \times 1]$ vector. The notation $(\cdot)_{A\to B}$ represents the range between A and B, delivered in a message from A or measured with a signal from A.

Similarly, the true local range between peer nodes and user u, $d_{n\to u}^{(k)}$, can be linearized around the predicted position $\hat{\mathbf{P}}_u^{-(k)}$ and expressed in terms of $\hat{d}_{n\to u}^{-(k)}$ and a small residual term as

$$\begin{aligned} d_{n\to u}^{(k)} &= \left.\sqrt{\left(x_u^{(k)}-x_n^{(k)}\right)^2+\left(y_u^{(k)}-y_n^{(k)}\right)^2+\left(z_u^{(k)}-z_n^{(k)}\right)^2}\right|_{\hat{\mathbf{P}}_u^{-(k)}} \\ &\simeq \hat{d}_{n\to u}^{-(k)} + \Delta_{\mathbf{P}_u}^{-(k)T}\left(\frac{\hat{\mathbf{P}}_u^{-(k)}-\mathbf{P}_n^{(k)}}{d_{n\to u}^{(k)}}\right) \\ &\simeq \hat{d}_{n\to u}^{-(k)} + \Delta_{\mathbf{P}_u}^{-(k)T}\mathbf{g}_n^{(k)} \end{aligned} \tag{9}$$

where the node direction vector $\mathbf{g}_n^{(k)} \simeq (\hat{\mathbf{P}}_u^{-(k)} - \mathbf{P}_n^{(k)})/\hat{d}_{n\to u}^{-(k)}$ is obtained using $d_{n\to u}^{(k)} \simeq \hat{d}_{n\to u}^{-(k)}$. Using (9), the set of M local ranges between M neighboring nodes and the user are found as follows:

$$\mathbf{r}_n^{(k)} \simeq \hat{\mathbf{d}}_n^{(k)} + \mathbf{G}_n^{(k)}\Delta_{\mathbf{P}_u}^{-(k)} + \mathbf{v}_n^{(k)} \tag{10}$$

where the m-th elements of $\mathbf{r}_n^{(k)}$, $\hat{\mathbf{d}}_n^{(k)}$, and $\mathbf{v}_n^{(k)}$ are $r_{n_m\to u}^{(k)}$, $\hat{d}_{n_m\to u}^{-(k)}$, and $v_{n_m\to u}^{(k)}$, respectively, and the m-th row of $\mathbf{G}_n^{(k)}$ is $\mathbf{g}_{n_m}^{(k)}$ for $m \in \{1, 2, \ldots, M\}$.

In this paper, depending on the use of differential correction for GNSS, we approximate the distribution of the pseudorange noise error $v_{s\to u}^{(k)}$ by a zero-mean Gaussian [2] as

$$v_{s\to u}^{(k)} \begin{cases} v_{d,s\to u}^{(k)} \sim \mathcal{N}\left(0, \sigma_{v_{d,s\to u}}^2\right), & \text{for DGNSS} \\ v_{g,s\to u}^{(k)} \sim \mathcal{N}\left(0, \sigma_{v_{g,s\to u}}^2\right), & \text{for GNSS.} \end{cases} \tag{11}$$

The pseudorange noise error for DGNSS $v_{d,s\to u}^{(k)}$ is caused by the noise in the received signal [2], and its variance is

$$\sigma_{v_{d,s_l\to u}}^2 = \frac{c^2 d_c T_c^2}{4T\left(\frac{C}{N_0}\right)_l} \tag{12}$$

where d_c is the correlator spacing used in the delay-locked loop (DLL) discriminator, T_c is the chip width, T is the integration time interval, and $(C/N_0)_l$ is the carrier-to-noise-density ratio (C/N_0) of the l-th satellite, whereas $v_{g,s\to u}^{(k)}$ includes the errors caused by the satellite clock, ephemeris error, and the ionosphere troposphere delays, as well as the noise in the received signal $\sigma_{v_{d,s_l\to u}}^2$. In addition, the local range noise errors $v_{u\to n}^{(k)}$ and $v_{n\to u}^{(k)}$ are assumed to have the same zero-mean Gaussian distribution as follows:

$$v_{u\to n}^{(k)}, v_{n\to u}^{(k)} \sim \mathcal{N}\left(0, \sigma_{v_{n\to u}}^2\right) \tag{13}$$

where $\sigma_{v_{n\to u}}$ is very small (less than 1 m) [22], [23].

III. Non-Line-of-Sight Detection Algorithm

NLOS propagation often involves a large delay that results in a large position error. Therefore, GNSS receivers in urban environments should inspect the measured pseudoranges of all satellites and mitigate the NLOS delays before fixing a position. Here, we propose an ND algorithm that performs a χ^2-test on the conditional statistics of the measured pseudoranges given the measured local ranges and possibly some measured pseudoranges that are from LOS signals. Exploiting [24], we assume that the predicted position error $\Delta_{\mathbf{P}_u}^{-(k)}$ is less than 1 m, which is much smaller than the NLOS delays observed in urban environments.

We define a combined range vector of size $[(L+M)\times 1]$ using $[L\times 1]$ vector $\boldsymbol{\rho}_s^{(k)}$ (8) and $[M\times 1]$ vector $\mathbf{r}_n^{(k)}$ (10) as

$$\boldsymbol{\zeta}^{(k)} = \begin{bmatrix} \boldsymbol{\rho}_s^{(k)} \\ \mathbf{r}_n^{(k)} \end{bmatrix} \tag{14a}$$

$$\simeq \hat{\mathbf{d}}'^{(k)} + \mathbf{G}^{(k)}\Delta_{\mathbf{P}_u}^{-(k)} + \mathbf{b}'^{(k)} + \mathbf{v}'^{(k)} + \boldsymbol{\tau}'^{(k)} \tag{14b}$$

where

$$\hat{\mathbf{d}}'^{(k)} = \left[\hat{\mathbf{d}}_s^{(k)T}\ \hat{\mathbf{d}}_n^{(k)T}\right]^T \tag{15a}$$

$$\mathbf{G}^{(k)} = \left[\mathbf{G}_s^{(k)T}\ \mathbf{G}_n^{(k)T}\right]^T \tag{15b}$$

$$\mathbf{b}'^{(k)} = \left[\mathbf{b}^{(k)T}\ \mathbf{O}_{1\times M}\right]^T \tag{15c}$$

$$\mathbf{v}'^{(k)} = \left[\mathbf{v}_s^{(k)T}\ \mathbf{v}_n^{(k)T}\right]^T \tag{15d}$$

$$\boldsymbol{\tau}'^{(k)} = \left[\boldsymbol{\tau}_{L_1\times 1}^{(k)T}\ \mathbf{O}_{1\times(M+L_2)}\right]^T \tag{15e}$$

where $\mathbf{O}_{1\times M} = [0, \ldots, 0]$ is a vector with M zeros, $\boldsymbol{\tau}_{L_1\times 1}^{(k)}$ is a row vector whose l_1-th element ($l_1 \in \{1, \ldots, L_1\}$) is $\tau_{l_1}^{(k)}$, M is the number of peer nodes connected to the user u, L is the total number of measured pseudoranges, L_1 is the true number of the measured pseudoranges corrupted by NLOS delays, and L_2 is the true number of measured pseudoranges not corrupted by NLOS delays. We drop the superscript '(k)' in the following because the proposed ND algorithm uses measurements and variables at the prompt. Because the five components constructing $\boldsymbol{\zeta}$ (14b) are independent and considering that $L+M$ elements are mutually independent, the distribution of the combined range vector is expressed as

$$\boldsymbol{\zeta} \sim \mathcal{N}(\mathbf{D}, \mathbf{V}) \tag{16}$$

where

$$\mathbf{D} = \hat{\mathbf{d}}' + \mathbf{b}' + \boldsymbol{\tau}' \tag{17a}$$

$$\mathbf{V} = \mathbf{G}\boldsymbol{\Lambda}\mathbf{G}^T + \boldsymbol{\Sigma}_{\boldsymbol{\zeta}} \tag{17b}$$

$\boldsymbol{\Lambda}$ is a $[3\times 3]$ diagonal matrix with diagonal elements $[\sigma_{\Delta_x^-}^2, \sigma_{\Delta_y^-}^2, \sigma_{\Delta_z^-}^2]$ that are the x, y, and z components of the predicted position error $\Delta_{\mathbf{P}_u}^-$, respectively, and $\boldsymbol{\Sigma}_{\boldsymbol{\zeta}}$ is a $[(L+M)\times(L+M)]$ diagonal noise error covariance matrix with a j-th diagonal element, i.e.,

$$\Sigma_{\boldsymbol{\zeta}}^{j,j} = \begin{cases} \sigma_{v_{s_j\to u}}^2, & \text{for } 1 \le j \le L \\ \sigma_{v_{n_{(j-L)}\to u}}^2, & \text{for } L+1 \le j \le L+M. \end{cases} \tag{18}$$

Since $\sigma^2_{\Delta_x^-} = \sigma^2_{\Delta_y^-} < 1$ m [24] and vehicles are on the same horizontal plane, we use

$$\sigma^2_{\Delta_x^-} = \sigma^2_{\Delta_y^-} = \sigma^2_{\Delta_z^-} = \sigma^2_{\Delta} \tag{19}$$

without a loss of generality.

In general, GNSS LOS signals have C/N_0 values higher than those of NLOS signals [25]. Therefore, the measured pseudoranges can be divided into two groups: group ϕ_1 for the measured pseudoranges to be tested to check for NLOS delays and group ϕ_2 for the measured pseudoranges that are expected to come from LOS using a threshold value of γ_{C/N_0} (> 40 dB-Hz). When $C/N_0 \geq \gamma_{C/N_0}$, the measured pseudorange is categorized into group ϕ_2; otherwise, it is categorized into group ϕ_1. It should be noted that ϕ_1 may include LOS signals and that ϕ_2 may not have any measured pseudorange when γ_{C/N_0} is too high (e.g., when $\gamma_{C/N_0} \gg 40$ dB-Hz); moreover, ϕ_2 always includes all of the measured local ranges that are assumed from LOS signals. It should also be noted that γ_{C/N_0} should be high enough that only LOS pseudoranges are in ϕ_2. In fact, the proposed ND algorithm performs successfully without any GNSS pseudorange in ϕ_2. The proposed algorithm shows robust performance when the number of measurements in ϕ_2, which is denoted N_{ϕ_2}, is greater than or equal to 2 ($N_{\phi_2} \geq 2$); the algorithm shows performance superior to that of the conventional RAIM [20], as demonstrated in Section V.

Let the measurements in ϕ_1 and ϕ_2 be denoted as $\boldsymbol{\zeta}_{\phi_1}$ and $\boldsymbol{\zeta}_{\phi_2}$, respectively, and be approximated by a Gaussian distribution as

$$\boldsymbol{\zeta} = \begin{bmatrix} \boldsymbol{\zeta}_{\phi_1} \\ \boldsymbol{\zeta}_{\phi_2} \end{bmatrix} \sim \mathcal{N}\left(\begin{bmatrix} \mathbf{D}_1 \\ \mathbf{D}_2 \end{bmatrix}, \begin{bmatrix} \mathbf{V}_{11} & \mathbf{V}_{12} \\ \mathbf{V}_{21} & \mathbf{V}_{22} \end{bmatrix} \right) \tag{20}$$

where $\mathbf{D}_1$ and $\mathbf{D}_2$ and the covariance matrices $\mathbf{V}_{11}$, $\mathbf{V}_{12}$, $\mathbf{V}_{21}$, and $\mathbf{V}_{22}$ are of size $[N_{\phi_1} \times 1]$, $[N_{\phi_2} \times 1]$, $[N_{\phi_1} \times N_{\phi_1}]$, $[N_{\phi_1} \times N_{\phi_2}]$, $[N_{\phi_2} \times N_{\phi_1}]$, and $[N_{\phi_2} \times N_{\phi_2}]$, respectively, and $N_{\phi_1} = \|\boldsymbol{\zeta}_{\phi_1}\|_0 \geq L_1$ and $N_{\phi_2} = \|\boldsymbol{\zeta}_{\phi_2}\|_0 \leq L_2 + M$. The measured pseudoranges in $\boldsymbol{\zeta}_{\phi_1}$ have a mean $\mathbf{D}_1$ and variance $\mathbf{V}_{11}$, and the measured pseudoranges and local ranges in $\boldsymbol{\zeta}_{\phi_2}$ have a mean $\mathbf{D}_2$ and variance $\mathbf{V}_{22}$.

When the measured pseudoranges in ϕ_1 are not corrupted by NLOS delays, the conditional variable $\boldsymbol{\zeta}_{\phi_1}|\boldsymbol{\zeta}_{\phi_2}$ has a conditional Gaussian distribution [26], with a mean and variance as

$$\boldsymbol{\mu}_{\phi_1} = \mathbf{D}_1 + \mathbf{V}_{12}\mathbf{V}_{22}^{-1}(\boldsymbol{\zeta}_{\phi_2} - \mathbf{D}_2) \tag{21a}$$

$$\mathbf{V}_{\phi_1} = \mathbf{V}_{11} - \mathbf{V}_{12}\mathbf{V}_{22}^{-1}\mathbf{V}_{21} \tag{21b}$$

respectively. Therefore, to check if the measured pseudoranges in ϕ_1 are corrupted by NLOS delays, we construct a normalized detection variable Z_{ϕ_1} that is the square of the Mahalanobis distance (MD) [27], i.e.,

$$Z_{\phi_1} = (\boldsymbol{\zeta}_{\phi_1} - \boldsymbol{\mu}_{\phi_1})^T \mathbf{V}_{\phi_1}^{-1}(\boldsymbol{\zeta}_{\phi_1} - \boldsymbol{\mu}_{\phi_1}). \tag{22}$$

The detection variable Z_{ϕ_1} has a noncentral χ^2 distribution with N_{ϕ_1} degrees of freedom (DOF) when the measured pseudoranges in ϕ_1 are corrupted by NLOS delays, and it has a central χ^2 distribution with N_{ϕ_1} DOF when the measured pseudoranges in ϕ_1 are from LOS signals.

It should be noted that the value of Z_{ϕ_1} in (22) is the sum of the MD squares of all the measured pseudoranges in ϕ_1, so that it is difficult to distinguish which of the measured pseudoranges is corrupted by an NLOS delay. Therefore, the proposed ND algorithm tests each of the measured pseudoranges in ϕ_1 individually. As a result, there are N_{ϕ_1} times 1 DOF χ^2-tests to be performed, which is computationally simple and efficient. Since

$$\sigma^2_{\Delta} + \Sigma^{j,j}_{\boldsymbol{\zeta}} > \sigma^2_{\Delta} \sum_{i \neq j} \left(\mathbf{g}_i^{(k)} \cdot \mathbf{g}_j^{(k)} \right) \tag{23}$$

the matrices $\mathbf{V}$ and $\mathbf{V}_{22}$ are strongly diagonally dominant matrices [28] for any $1 \leq i, j \leq L + M$ and $i \neq j$. Therefore, the determinants of $\mathbf{V}$ and $\mathbf{V}_{22}$ can be approximated by the product of the diagonal elements of the matrices [28]; it is found that

$$|\mathbf{V}_{\phi_1}| = \left|\mathbf{V}_{11} - \mathbf{V}_{12}\mathbf{V}_{22}^{-1}\mathbf{V}_{21}\right|$$

$$= \frac{|\mathbf{V}|}{|\mathbf{V}_{22}|} \tag{24a}$$

$$\approx \mathbf{V}_{11} \tag{24b}$$

$$= \sigma^2_{\Delta} + \sigma^2_{v_{s \to u}} \tag{24c}$$

where $\mathbf{V}_{11}$ is of size $[1 \times 1]$, (24a) is from [29], and (24b) is from [28].

When the detection variable Z_{ϕ_1} is larger than a certain detection threshold γ_t (≥ 2, in general), we conclude that the measured pseudorange is corrupted by NLOS delay. Since Z_{ϕ_1} (22) can be obtained from a simple numerical evaluation, the computational cost for the proposed ND algorithm is negligibly small, which is a strong advantage over the conventional statistics-based outlier detection techniques such as RAIM [20]. In addition, as shown in Section V, the detection probability P_D and false alarm probability P_F of the proposed ND algorithm are much better than those of robust RAIM techniques using MM-estimator and L_1-norm algorithms [20]; The robust RAIM techniques have $P_D \leq 0.65$ when just two NLOS satellite signals are present, whereas the proposed ND algorithm has $P_D \geq 0.8$, as shown in Fig. 6.

IV. Proposed Multipath-Resistant Techniques

Here, we consider two conventional CP techniques, i.e., hcEKF and H-SPAWN, that are based on EKF and BP, respectively. The hcEKF technique is one of the most computationally efficient and widely used techniques, and the H-SPAWN technique provides highly accurate (near-optimal) position estimation using the low-computational BP algorithm for Bayesian inference problems with sensor fusion that is modeled by a Bayesian network. Exploiting the proposed ND algorithm in Section III, we propose the MRH-SPAWN technique in Section IV-A and the MR-hcEKF technique in Section IV-B; these are enhanced techniques of H-SPAWN and hcEKF,

respectively, for GNSS multipath. While the MR-hcEKF technique is easily designed by integrating the proposed ND algorithm and hcEKF, the MRH-SPAWN technique does not emerge in a straightforward manner from the H-SPAWN; for this reason, we provide the derivation in detail.

A. MRH-SPAWN

In Section IV-A1, we introduce the Bayesian inference for the cooperative vehicular navigation systems [13] and [15]. The proposed ND algorithm is applied to the CP system on a factor graph [14] using the sum–product algorithm (SPA) [14] in Section IV-A2. In Section IV-A3, messages used in the proposed technique are described.

1) Bayesian Inference: Exploiting [15] and [30], the *a posteriori* distribution of user u is expressed as

$$p\left(\mathbf{x}_u^{(k)}|\mathbf{\Gamma}_U^{(1:k)}, \boldsymbol{R}_U^{(1:k)}\right) \tag{25}$$

where $\mathbf{\Gamma}_U^{(1:k)}$ denotes the measured pseudoranges in U (i.e., $\mathbf{\Gamma}_U^{(k)} \triangleq \{\boldsymbol{\rho}_u^{(k)}|\forall\, u \in U\}$) from time instant t_1 to t_k, and $\boldsymbol{R}_U^{(1:k)}$ represents the measured local ranges in U (i.e., $\boldsymbol{R}_U^{(k)} \triangleq \{\mathbf{r}_u^{(k)}|\ \forall\, u \in U\}$) from time instant t_1 to t_k.

Assuming a system dynamic model that follows the Markov process [26] and the conditional independence between the measured pseudoranges and the measured local ranges, the factorized joint *a posteriori* distribution (25) of state $\mathbf{x}_u^{(k)}$ is found to be [15]

$$\begin{aligned} &p\left(\mathbf{\Gamma}_U^{(k)}|\boldsymbol{X}_U^{(k)}\right) p\left(\boldsymbol{R}_U^{(k)}|\boldsymbol{X}_U^{(k)}\right) \prod_{u\in U} p\left(\mathbf{x}_u^{(k)}|\mathbf{x}_u^{(k-1)}\right) \\ &= \prod_{u=1}^{U}\left[F_u\left(\mathbf{x}_u^{(k)}, \mathbf{x}_u^{(k-1)}\right) \prod_{s\in S_u} T_u^s\left(\mathbf{x}_u^{(k)}\right) \prod_{\substack{n\in U_u \\ n<u}} H_u^n\left(\mathbf{x}_u^{(k)}, \mathbf{x}_n^{(k)}\right)\right] \end{aligned} \tag{26}$$

where

$$\boldsymbol{X}_U^{(k)} \triangleq \left\{\mathbf{x}_u^{(k)}|\forall\, u \in U\right\} \tag{27a}$$

$$F_u\left(\mathbf{x}_u^{(k)}, \mathbf{x}_u^{(k-1)}\right) = p\left(\mathbf{x}_u^{(k)}|\mathbf{x}_u^{(k-1)}\right) \tag{27b}$$

$$T_u^s\left(\mathbf{x}_u^{(k)}\right) = p\left(\rho_{s\to u}|\mathbf{x}_u^{(k)}\right) \tag{27c}$$

$$H_u^n\left(\mathbf{x}_u^{(k)}, \mathbf{x}_n^{(k)}\right) = p\left(r_{n\to u}|\mathbf{x}_u^{(k)}, \mathbf{x}_n^{(k)}\right) \tag{27d}$$

represent the state vector of all nodes, the system dynamics, the pseudorange measurement likelihood, and the local range measurement likelihood, respectively. Therefore, the factorized recursive Bayesian inference problem can be expressed on a factor graph, and the *a posteriori* distribution can be easily calculated using the SPA. However, since any measured pseudorange may be corrupted by an NLOS delay, we should perform the proposed ND algorithm before estimating the state $\mathbf{x}_u^{(k)}$.

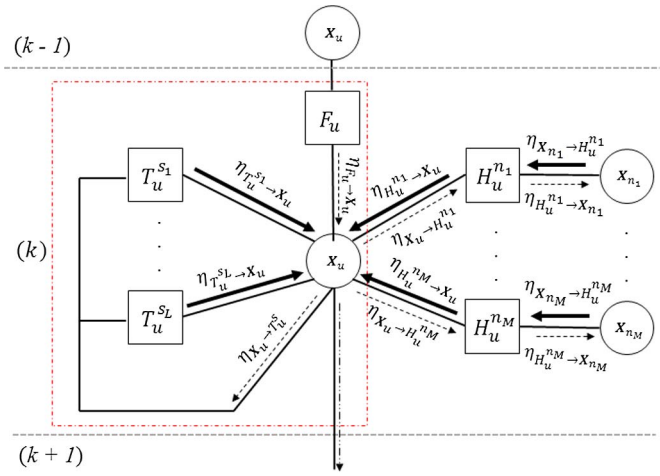

Fig. 3. Factor graph for the proposed MRH-SPAWN technique. Dashed box indicates a physical vehicle unit.

TABLE I
PROPOSED MRH-SPAWN TECHNIQUE

Input: Initial estimated state $\hat{p}\left(\mathbf{x}_u^{(0)}\right)$
Output: Update marginal estimate state $\hat{p}\left(\mathbf{x}_u^{(k)}\right)$
1: ***for*** *time instant* $k = 1$ *to* K
2: $\forall u \in U$:
3: Compute prediction message : $\eta_{F_u\to\mathbf{x}_u}$ (28)
4: Compute feedback message : $\eta_{\mathbf{x}_u\to T_u^s} = \eta_{F_u\to\mathbf{x}_u}$
5: Broadcast to peer node: $\eta_{\mathbf{x}_u\to H_u^n} = \eta_{F_u\to\mathbf{x}_u}$
6: Receive measurements and information:
7: $\rho_{s\to u}^{(k)}, \mathrm{C/N}_0^{(k)}, \mathbf{P}_s^{(k)}$ for $s \in S_u^{(k)}$
8: and $r_{n\to u}^{(k)}$ for $n \in U_u^{(k)}$
9: ***for*** *iteration* $i = 1$ *to* I
10: ***for*** *node* $u = 1$ *to* U *in parallel*
11: Receive peer node message: $\eta_{\mathbf{x}_n\to H_u^n}$
12: Compute peer node message: $\eta_{H_u^n\to\mathbf{x}_u}$ (34)
13: Compute satellite message: $\eta_{T_u^s\to\mathbf{x}_u}$ (33)
14: Broadcast to peer: $\eta_{\mathbf{x}_u\to H_u^n}$ (36)
15: Compute feedback message: $\eta_{\mathbf{x}_u\to T_u^s}$ (38), (39)
16: Update $\hat{p}\left(\mathbf{x}_u^{(k)}\right)$. (38), (39)
17: ***end for***
18: ***end for***
19:***end for***

2) MRH-SPAWN on Factor Graph and Message-Passing Algorithm: We show the proposed MRH-SPAWN technique on a factor graph in Fig. 3 and summarize the message passing algorithm in Table I. We denote a message from node A to node B as $\eta_{A\to B}$.

The procedure of the MRH-SPAWN message-passing algorithm consists of two parts: time steps to update messages using the previously estimated state and new measurements (shown in Table I, lines 2 to 8), and iteration steps within each time step estimate $\mathbf{x}_u^{(k)}$ (shown in Table I, lines 10–17). The messages used in the MRH-SPAWN are the prediction and measurement likelihood messages for state estimation, broadcast messages to peer nodes, received messages from the peer nodes, and a feedback message for the proposed ND algorithm.

The MRH-SPAWN message-passing algorithm starts from time step $k = 1$. As shown in Fig. 3, at each time step k, the factor node F_u computes the prediction message $\eta_{F_u\to\mathbf{x}_u}$ (shown in Table I, line 3), which includes the information about the distribution of the predicted state $\hat{\mathbf{x}}_u^{-(k)}$ (1b), from

which the feedback is updated as $\eta_{\mathbf{x}_u \to T_u^s} = \eta_{F_u \to \mathbf{x}_u}$ (shown in Table I, lines 4). Since the proposed ND algorithm is performed in each satellite factor node $T_u^{s_l}$ $(l \in \{1, 2, \ldots, L\})$, the feedback message should pass to the factor node $T_u^{s_l}$ only. The broadcast messages are updated as $\eta_{\mathbf{x}_u \to H_u^n} = \eta_{F_u \to \mathbf{x}_u}$ so that every peer nodes can utilize the message. The dashed arrows in Fig. 3 show the propagation of the feedback and the broadcast messages before the iteration stage starts. The measurements $(\rho_{s\to u}^{(k)}, r_{n\to u}^{(k)})$ and information $(C/N_0^{(k)}, \mathbf{P}_s^{(k)})$ for the proposed ND algorithm are updated at every time steps. In the iteration step, the message from the m-th peer node $\eta_{H_u^{n_m} \to \mathbf{x}_u}$ is computed at the factor node $H_u^{n_m}$ (shown in Table I, line 12) using the received message from the peer node m; $\eta_{\mathbf{x}_{n_m} \to H_u^{n_m}}$ (shown in Table I, line 11). The message from the m-th peer node $\eta_{H_u^{n_m} \to \mathbf{x}_u}$ provides the likelihood of the local range measurement (27d).

The satellite message of the l-th satellite $\eta_{T_u^{s_l} \to \mathbf{x}_u}$ provides the likelihood of the pseudorange measurement (27c) whose uncertainty is updated by the proposed ND algorithm. The satellite message $\eta_{T_u^{s_l} \to \mathbf{x}_u}$ is computed at the factor node $T_u^{s_l}$ (shown in Table I, line 13) using the proposed ND algorithm based on the pseudorange measurements and satellite information ($\rho_{s\to u}^{(k)}$, $\mathbf{P}_s^{(k)}$, $\sigma_{v_{s\to u}}^2$, and $C/N_0^{(k)}$) and the range measurements and peer node information ($r_{n\to u}^{(k)}$, $\mathbf{P}_n^{(k)}$, and $\sigma_{v_{n\to u}}^2$), where $\mathbf{P}_n^{(k)}$ is from the received message $\eta_{\mathbf{x}_n \to H_u^n}$ (shown in Table I, lines 7, 8, and 11). The information required for the proposed ND algorithm is available from the factor node T_u^s, and the proposed ND algorithm produces detection variable Z_{ϕ_1} for each satellite in ϕ_1. Since a measured pseudorange with larger NLOS delay should be deweighted in the position estimation, we weight the noise variance of the measured pseudorange by the detection variable. Therefore, the satellite message $\eta_{T_u^{s_l} \to \mathbf{x}_u}$ is deweighted Z_{ϕ_1} times. When the measured pseudorange is not corrupted by NLOS delay, we set the weight factor to 1. The details of the message computation are introduced in Section IV-A3. The flow of the likelihood messages updated at the factor nodes is shown with bold arrows in Fig. 3.

The broadcast message $\eta_{\mathbf{x}_u \to H_u^n}$ and the feedback message $\eta_{\mathbf{x}_u \to T_u^s}$ are updated at each iteration based on the conventional SPA [14] using likelihoods (36) and (38) (shown in Table I, lines 14 and 15). When the messages converge, we conclude that the MRH-SPAWN technique has obtained the final marginal *a posteriori* state estimate $\hat{p}(\mathbf{x}_u)$ by multiplying by all the incoming messages to the variable node $\mathbf{x}_u$ (26) (shown in Table I, line 16), and the procedure follows the dashed-dot arrow to the next time instant $k+1$ at the completion of the iteration stage (i.e., $i = I$) for the current time instant k, as shown in Fig. 3.

3) Message Distributions: Here, we define the messages for the MRH-SPAWN in Fig. 3. We introduce principle expressions briefly but provide in detail description of the new messages modified from [15], and the messages are expressed using a parametric BP strategy and approximated by the known "distribution families" as in [15].

a) Prediction message: The prediction message is updated using the SPA algorithm [14] to represent the distribution of the predicted state $\hat{\mathbf{x}}_u^{-(k)}$ (1b) using the previous state. This message is used for message updates and the proposed ND algorithm. Exploiting [15], we approximate the state prediction message by a Gaussian probability distribution function (pdf) as follows:

$$\begin{aligned}\eta_{F_u \to \mathbf{x}_u^{(k)}}\left(\mathbf{x}_u^{(k)}\right) &\approx \mathcal{N}\left(\mathbf{x}_u^{(k)}; \boldsymbol{\mu}_{\mathbf{x}_u^{(k)}}, \boldsymbol{\Sigma}_{\mathbf{x}_u^{(k)}}\right) \\ &= \frac{1}{\lambda} e^{-\frac{1}{2}\left(\mathbf{x}_u^{(k)} - \boldsymbol{\mu}_{\mathbf{x}_u^{(k)}}\right)^T \boldsymbol{\Sigma}_{\mathbf{x}_u^{(k)}}^{-1} \left(\mathbf{x}_u^{(k)} - \boldsymbol{\mu}_{\mathbf{x}_u^{(k)}}\right)}\end{aligned} \tag{28}$$

where $\boldsymbol{\mu}_{\mathbf{x}_u^{(k)}}$, $\boldsymbol{\Sigma}_{\mathbf{x}_u^{(k)}}$, and λ denote the mean and covariance matrices of the state $\mathbf{x}^{(k)}$, and a normalization factor, respectively. Moreover, $\mathcal{N}(y; m_y, \sigma_y^2)$ represents a Gaussian pdf of a variable y with a mean m_y and a variance σ_y^2.

b) Satellite message: The satellite message is an output of the proposed ND algorithm and may be refined using the MD used as a weight factor. As in Fig. 3, the satellite message is computed, for every iteration $i (1 \le i \le I)$ of the MRH-SPAWN, using SPA as

$$\eta_{T_u^s \to \mathbf{x}_u^{(k)}}\left(\mathbf{x}_u^{(k)}\right) \propto \int T_u^s\left(\mathbf{x}_u^{(k)}\right) \eta_{\mathbf{x}_u^{(k)} \to T_u^s}\left(\mathbf{x}_u^{(k)}\right) \partial \mathbf{x}_u^{(k)}. \tag{29}$$

Exploiting the analysis in [15], the satellite message is computed as

$$\begin{aligned}\eta_{T_u^s \to \mathbf{x}_u^{(k)}}\left(\mathbf{x}_u^{(k)}\right) &= p_V\left(\mathbf{x}_u^{(k)}; \rho_{s\to u}^{(k)}, \mathbf{P}_s^{(k)}, \sigma_{v_{s\to u}}^2\right) \\ &= \frac{1}{\lambda} \exp\left[-\frac{\left(\left\|\mathbf{P}_u^{(k)} - \mathbf{P}_s^{(k)}\right\| + b_u^{(k)} - \rho_{s\to u}^{(k)}\right)^2}{2\sigma_{v_{s\to u}}^2}\right]\end{aligned} \tag{30}$$

where $\rho_{s\to u}^{(k)}$, $\mathbf{P}_s^{(k)}$, $\sigma_{v_{s\to u}}^2$, and λ are the measured pseudorange, the satellite position, the pseudorange noise variance, and a normalization factor, respectively. The pdf $p_V(\cdot)$ (30) is a hyper-conic distribution family that cannot be approximated by a Gaussian pdf due to the clock bias $b^{(k)}$ [15].

In MRH-SPAWN, we do not compute (30) before the proposed ND algorithm is performed at each factor node $T_u^{s_l}$ $(l = 1, 2, \ldots, L)$, and we produce the weight factor w_l as

$$w_l = \begin{cases} Z_{\phi_{1l}}, & \text{for } Z_{\phi_{1l}} > \gamma_t \\ 1, & \text{for } Z_{\phi_{1l}} \le \gamma_t \text{ or } l \in \phi_2 \end{cases} \tag{31}$$

where $l \in \{1, \ldots, L\}$ is the satellite index. It should be noted that the input to the proposed ND algorithm are the satellite information, such as $\rho_{s\to u}^{(k)}$, $\mathbf{P}_s^{(k)}$, $\sigma_{v_{s\to u}}^2$, and $C/N_0^{(k)}$, and the peer node information, such as $r_{n\to u}^{(k)}$, $\mathbf{P}_n^{(k)}$, and $\sigma_{v_{n\to u}}^2$, where $\mathbf{P}_n^{(k)}$ can be obtained from the received message $\eta_{\mathbf{x}_n \to H_u^n}$. Using w_l, we weight the pseudorange noise variance as

$$\sigma_{v_{s_l\to u}}^{*2} = w_l \times \sigma_{v_{s_l\to u}}^2 \tag{32}$$

so that the refined satellite message of (30) becomes

$$\eta_{T_u^s \to \mathbf{x}_u^{(k)}}\left(\mathbf{x}_u^{(k)}\right) = p_V\left(\mathbf{x}_u^{(k)}; \rho_{s\to u}^{(k)}, \mathbf{P}_s^{(k)}, \sigma_{v_{s\to u}}^{*2}\right). \quad (33)$$

It should be noted that (33) increases the uncertainty of the measured pseudorange corrupted by NLOS delay using the weight factor w_l so that the message from the NLOS satellite contributes less to the position estimation.

c) Peer node message: The peer node message $\eta_{H_u^n \to \mathbf{x}_u^{(k)}}$ provides the likelihood of the local range measurement $p(\rho_{s\to u}|\mathbf{x}_u^{(k)})$ based on the mean and variance of the peer's estimated position. The peer node message $\eta_{H_u^n \to \mathbf{x}_u^{(k)}}$ can be computed following the SPA update rule [14] and is modeled as [15]:

$$\eta_{H_u^n \to \mathbf{x}_u^{(k)}}\left(\mathbf{x}_u^{(k)}\right) = p_C\left(\mathbf{x}_u^{(k)}; r_{n\to u}^{(k)}, \mu_{\mathbf{P}_{n\to u}^{(k)}}, \Sigma_{\mathbf{P}_{n\to u}^{(k)}} + \sigma_{v_{n\to u}}^2 I\right) \quad (34)$$

where $p_C(\cdot)$ is the cylindrical distribution [15] such that

$$p_C\left(\mathbf{x}; r, \boldsymbol{\mu}_{\mathbf{P}_n}, \boldsymbol{\Sigma}_{\mathbf{P}_{n+r}}\right) = \frac{1}{\lambda}\exp\left[-\frac{1}{2}\left(\mathbf{p}' - r\frac{\mathbf{p}'}{\|\mathbf{p}'\|}\right)^T \boldsymbol{\Sigma}_{\mathbf{p}_{n+r}}^{-1}\left(\mathbf{p}' - r\frac{\mathbf{p}'}{\|\mathbf{p}'\|}\right)\right] \quad (35)$$

where $\boldsymbol{\mu}_{\mathbf{P}_{n\to u}^{(k)}}$ and $\boldsymbol{\Sigma}_{\mathbf{P}_{n\to u}^{(k)}}$ denote the mean and variance matrices, respectively, of the message $\eta_{\mathbf{x}_n^{(k)} \to H_u^n}$; $\mathbf{p}' = \mathbf{p}_u - \boldsymbol{\mu}_{\mathbf{p}_n}$; and λ is a normalization factor.

d) Broadcast message to peer nodes: For the positioning of the peer node n, the user u broadcasts a message $\eta_{\mathbf{x}_u^{(k)} \to H_u^n}$. The message from the user u to the peer node factor H_u^n is computed using the SPA [14]. By exploiting [15], the message is approximated by a Gaussian distribution as follows:

$$\eta_{\mathbf{x}_u^{(k)} \to H_u^n}\left(\mathbf{x}_u^{(k)}\right) \approx \mathcal{N}\left(\mathbf{x}_u^{(k)}; \boldsymbol{\mu}_{\mathbf{x}_{u\to n}^{(k)}}, \boldsymbol{\Sigma}_{\mathbf{x}_{u\to n}^{(k)}}\right) \quad (36)$$

and the parameters $\boldsymbol{\mu}_{\mathbf{x}_{u\to n}^{(k)}}$ and $\boldsymbol{\Sigma}_{\mathbf{x}_{u\to n}^{(k)}}$ can be obtained using the parameter estimation algorithm inspired from the importance sampling [15] as follows:

$$\hat{\boldsymbol{\mu}}_{\mathbf{x}} = \sum_{q=1}^{N} W_q \mathbf{z}_q \quad (37a)$$

$$\hat{\boldsymbol{\Sigma}}_{\mathbf{x}} = \frac{\sum_{q=1}^{N} W_q (\mathbf{z}_q - \hat{\boldsymbol{\mu}}_x)(\mathbf{z}_q - \hat{\boldsymbol{\mu}}_{\mathbf{x}})^T}{1 - \sum_{q=1}^{N} W_q^2} \quad (37b)$$

where $\mathbf{z}_q$ denotes the q-th sample from the current estimated distribution of $\hat{p}(\mathbf{x}_u^{(k)})$ computed at each iteration (shown in Table I, line 16), and W_q denotes the q-th sample's weight determined by the product of the probability of the incoming message; $\eta_{F_u \to \mathbf{x}_u^{(k)}}$, $\eta_{T_u^s \to \mathbf{x}_u^{(k)}}$, and $\eta_{H_u^n \to \mathbf{x}_u^{(k)}}$.

e) Feedback message and state estimation: The feedback message $\eta_{\mathbf{x}_u^{(k)} \to T_u^s}$, which is used for the proposed ND algorithm and the marginal *a posteriori* distribution $\hat{p}(\mathbf{x}_u^{(k)})$, is computed by multiplying by all of the messages to the user u as

$$\eta_{\mathbf{x}_u^{(k)} \to T_u^s}\left(\mathbf{x}_u^{(k)}\right), \hat{p}\left(\mathbf{x}_u^{(k)}\right) \propto \eta_{F_u \to \mathbf{x}_u^{(k)}}\left(\mathbf{x}_u^{(k)}\right) \times \prod_{s\in S_u^{(k)}} \eta_{T_u^s \to \mathbf{x}_u^{(k)}}\left(\mathbf{x}_u^{(k)}\right) \prod_{l\in U_u^{(k)}} \eta_{H_u^n \to \mathbf{x}_u^{(k)}}\left(\mathbf{x}_u^{(k)}\right). \quad (38)$$

It should be noted that the feedback message $\eta_{\mathbf{x}_u \to T_u^s}$ is updated at each iteration step, whereas the marginal *a posteriori* distribution $\hat{p}(\mathbf{x}_u^{(k)})$ is computed after the convergence of all messages. By exploiting [15], $\eta_{\mathbf{x}_u \to T_u^s}$ and $\hat{p}(\mathbf{x}_u^{(k)})$ are approximated by a Gaussian distribution as follows:

$$\eta_{\mathbf{x}_u \to T_u^s}\left(\mathbf{x}_u^{(k)}\right), \hat{p}\left(\mathbf{x}_u^{(k)}\right) \approx \mathcal{N}\left(\mathbf{x}_u^{(k)}; \hat{\boldsymbol{\mu}}_{\mathbf{x}_u^{(k)}}, \hat{\boldsymbol{\Sigma}}_{\mathbf{x}_u^{(k)}}\right) \quad (39)$$

where the parameters $\hat{\boldsymbol{\mu}}_{\mathbf{x}_u^{(k)}}$ and $\hat{\boldsymbol{\Sigma}}_{\mathbf{x}_u^{(k)}}$ are obtained from (37a) and (37b).

B. MR-hcEKF

Here, we introduce the principle of the hcEKF technique [10] briefly, and we integrate the proposed ND algorithm into the hcEKF to propose the MR-hcEKF technique.

1) Time Update Step: A priori state $\hat{\mathbf{x}}_u^{-(k)}$ is updated using vehicle dynamics $f(\cdot)$, and *a priori* covariance $\boldsymbol{\Sigma}_{\hat{\mathbf{x}}_u^{-(k)}}$ is updated using the previous *a posteriori* covariance $\boldsymbol{\Sigma}_{\hat{\mathbf{x}}_u^{(k-1)}}$ and the system noise covariance $\boldsymbol{\Sigma}_f^{(k)}$. The *a priori* state and the *a priori* covariance are expressed as

$$\hat{\mathbf{x}}_u^{-(k)} = f\left(\hat{\mathbf{x}}_u^{(k-1)}\right) \quad (40)$$

$$\boldsymbol{\Sigma}_{\hat{\mathbf{x}}_u^{-(k)}} = \mathbf{A}^{(k)} \boldsymbol{\Sigma}_{\hat{\mathbf{x}}_u^{(k-1)}} \mathbf{A}^{(k)T} + \mathbf{W}^{(k)} \boldsymbol{\Sigma}_f^{(k)} \mathbf{W}^{(k)T} \quad (41)$$

where the system Jacobian matrices are

$$\mathbf{A}^{(k)} = \left.\frac{\partial f}{\partial \mathbf{x}_u}\right|_{\hat{\mathbf{x}}_u^{(k-1)}}, \mathbf{W}^{(k)} = \left.\frac{\partial f}{\partial \mathbf{w}_u}\right|_{\hat{\mathbf{x}}_u^{(k-1)}}. \quad (42)$$

2) Measurement Update Step: In this step, the Kalman gain $\mathbf{K}^{(k)}$, *a posteriori* state $\hat{\mathbf{x}}_u^{(k)}$, and covariance $\boldsymbol{\Sigma}_{\hat{\mathbf{x}}_u^{(k)}}$ are computed using the measurement $\boldsymbol{\zeta}^{(k)}$ (14a), measurement model $h(\cdot)$, measurement noise covariance $\boldsymbol{\Sigma}_{\boldsymbol{\zeta}}^{(k)}$ (18), and *a priori* state covariance $\boldsymbol{\Sigma}_{\hat{\mathbf{x}}_u^{-(k)}}$ as

$$\mathbf{K}^{(k)} = \boldsymbol{\Sigma}_{\hat{\mathbf{x}}_u^{-(k)}} \mathbf{H}^{(k)T}\left(\mathbf{H}^{(k)} \boldsymbol{\Sigma}_{\hat{\mathbf{x}}_u^{-(k)}} \mathbf{H}^{(k)T} + \mathbf{V}^{(k)} \boldsymbol{\Sigma}_{\boldsymbol{\zeta}^{(k)}} \mathbf{V}^{(k)T}\right)^{-1} \quad (43)$$

$$\hat{\mathbf{x}}_u^{(k)} = \hat{\mathbf{x}}_u^{-(k)} + \mathbf{K}^{(k)}\left(\boldsymbol{\zeta}^{(k)} - h\left(\hat{\mathbf{x}}_u^{-(k)}, \mathbf{P}_s^{(k)}, \hat{\mathbf{P}}_n^{(k)}\right)\right) \quad (44)$$

$$\boldsymbol{\Sigma}_{\hat{\mathbf{x}}_u^{(k)}} = \left(\mathbf{I} - \mathbf{K}^{(k)} \mathbf{H}^{(k)}\right) \boldsymbol{\Sigma}_{\hat{\mathbf{x}}_u^{-(k)}} \quad (45)$$

where the measurement Jacobian matrices are

$$\mathbf{H}^{(k)} = \left.\frac{\partial h}{\partial \mathbf{x}_u}\right|_{\hat{\mathbf{x}}_u^{-(k)}}, \mathbf{V}^{(k)} = \left.\frac{\partial h}{\partial \mathbf{v}_u}\right|_{\hat{\mathbf{x}}_u^{-(k)}}. \quad (46)$$

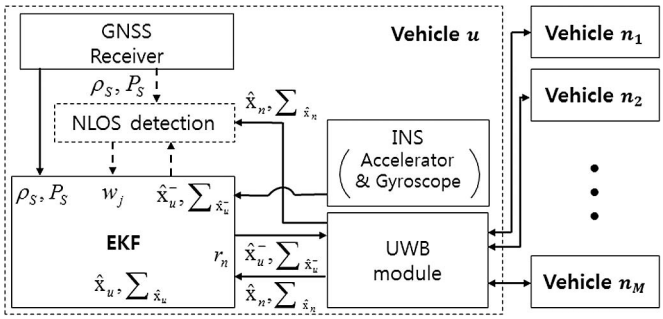

Fig. 4. Proposed MR-hcEKF technique.

To apply the proposed ND algorithm to hcEKF, the j-th diagonal element of the measurement noise covariance matrix $\mathbf{\Sigma}_{\boldsymbol{\zeta}}$ is computed as

$$\Sigma_{\boldsymbol{\zeta}}^{j,j} = \begin{cases} w_j \sigma^2_{v_{s_j \to u}}, & \text{for } 1 \le j \le L \\ \sigma^2_{v_{n_{(j-L)} \to u}}, & \text{for } L+1 \le j \le L+M \end{cases} \tag{47}$$

where L and M are the total numbers of the measured pseudoranges and the measured local ranges, respectively. Similar to the case of MRH-SPAWN, NLOS effects in this case can be reduced by increasing the uncertainty of the detected NLOS signals by utilizing the weight factor w_j. Fig. 4 provides a diagram of the proposed MR-hcEKF technique.

V. Performance Analysis and Simulation Results

We demonstrate the performance of the proposed ND algorithm in Section V-A and of the proposed techniques MR-hcEKF and MRH-SPAWN using numerous Monte Carlo simulations with empirical multipath errors observed in the field for typical urban scenarios in Section V-B.

A. Performance of the Proposed ND Algorithm

To demonstrate the performance of the proposed ND algorithm, we perform 10^4 Monte Carlo simulations for various multipath delays. In the simulations, the error of the predicted state $\hat{\mathbf{x}}_u^{-(k)}$ consists of the error from the predicted position $\hat{\mathbf{P}}_u^{-(k)}$ and the error from the predicted clock bias $\hat{b}^{-(k)}$, where both errors are expressed as Gaussian distributions with standard deviations of σ_Δ (19) and σ_b, respectively. The following describes the simulation conditions based on field observations.

- Satellites are uniformly distributed in the sky above a small elevation angle of 10°, and peer nodes are uniformly distributed on an xy-horizontal plane relative to the user.
- Peer vehicles are on the horizontal plane, and their azimuth angles are uniformly distributed at $[0, 360°)$.
- Satellite signals in ϕ_1 and ϕ_2 have C/N_0's uniformly distributed at [30, 40] and [40, 48] dB-Hz, respectively, and $\gamma_{C/N_0} = 42$ dB-Hz is used.
- The value of ϕ_1 includes one measured pseudorange from an LOS signal whose C/N_0 is less than 40 dB-Hz, when there is more than one measurement from a LOS signal in ϕ_2.

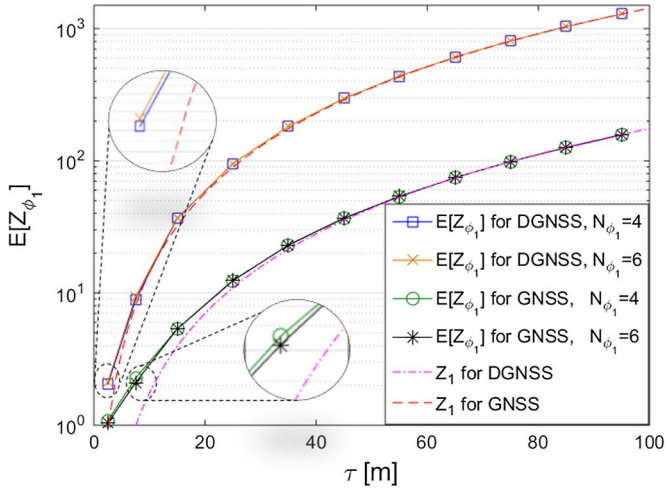

Fig. 5. Average detection variable $E[Z_{\phi_1}]$ and Z_1 versus the NLOS delay τ.

- Based on the empirical data in [24], where $\sigma_{\Delta_x^-} \le 1$ m and $\sigma_{\Delta_y^-} \le 1$ m, we use $\sigma_\Delta = 1$ m and $\sigma_b = 1$ m.
- For measurement noise, we use slightly larger values than those in the empirical data, as introduced in [2] and [31]: $\sigma_{v_{g,s_l \to u}} = 7.5$ m for GNSS, $\sigma_{v_{d,s_l \to u}} = 2.5$ m for DGNSS, and $\sigma_{v_{n_l \to u}} = 1$ m for local ranging.

Fig. 5 shows the average MD squares, i.e., $E[Z_{\phi_1}]$, observed in the Monte Carlo simulations versus the NLOS delay τ in meters. In addition, the approximate theoretical model of the 1-D MD squares is found using (22) and (24c) as

$$Z_1 = \frac{\tau^2}{\sigma_\Delta^2 + \Sigma_\zeta^{1,1}}. \tag{48}$$

In Fig. 5, we show $E[Z_{\phi_1}]$ and Z_1 (48) for various N_{ϕ_1} and for GNSS and DGNSS receivers with respect to the NLOS delay. Because the pseudorange noise variance of DGNSS is much smaller than that of GNSS, the result shows that $E[Z_{\phi_1}]$ and Z_1 of DGNSS are much larger than those of GNSS. It should be noted that N_{ϕ_1} has no effect on the proposed ND algorithm as the algorithm tests the measured pseudoranges in ϕ_1 individually. In Fig. 5, we can find that, for example, $\tau = 10$ m results in $E[Z_{\phi_1}] \approx 20$ for DGNSS and $E[Z_{\phi_1}] \approx 4$ for GNSS, which shows that cooperative vehicles with DGNSS receivers can detect NLOS multipath delays much better than such vehicles with GNSS receivers.

Fig. 6 provides a graph of the detection probability P_D and the false alarm probability P_F with respect to the NLOS delay detection threshold γ_τ for NLOS delays with a mean of 30 m and a standard deviation of 10 m, where P_D and P_F are from [32]. As shown, the probabilities from the numerous Monte Carlo simulations are in good agreement with those from the theoretical analysis, and as expected, P_F decreases rapidly and does not depend on the distribution of the NLOS delays, whereas P_D starts to decrease when γ_τ exceeds the mean of the NLOS delay distribution. However, the distribution of NLOS delays is difficult to determine as it depends on the local environments and objects around the connected vehicles. Therefore, in practice, we use γ_t, which results in a very

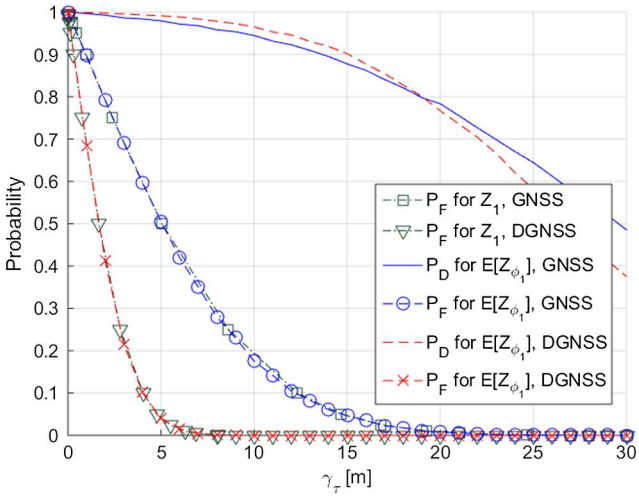

Fig. 6. Probabilities of detection P_D and false alarm P_F for GNSS and DGNSS.

low constant false alarm rate (CFAR). Since the detection variable, i.e., the MD squares, $E[Z_{\phi_1}]$ has a χ^2 distribution with one DOF, $P_F \leq 0.01$ (i.e., less than 1%) can be achieved with $\gamma_t = 6.625$ [32]. It turns out that, based on (48) NLOS delays larger than $\tau \simeq 19$ m, and $\tau \simeq 7.5$ m can be detected by GNSS and DGNSS receivers, respectively, as shown in Fig. 6. In the following performance simulations, we use detection thresholds $\gamma_\tau = 19$ m and $\gamma_\tau = 7.5$ m for vehicles with GNSS and DGNSS receivers, respectively.

B. NLOS Delay Distribution

To verify the actual performance of the proposed ND algorithm and the proposed techniques, knowledge of the NLOS delay distribution in an urban street environments is necessary. One of the statistical GNSS channel models based on massive empirical data is the land mobile satellite channel (LMSC) model, recommended by the International Telecommunication Union (ITU) for mobile GNSS channels and standardized in ITU-R P.681-7 [33]. In this model, virtual urban canyons are constructed along a road, with buildings, trees, and poles on both sides of the road; channel impulse responses are then generated based on the ray-tracing method. The size, height, interval, and appearance frequency of the buildings, trees, and poles are determined by the input parameters. We use typical parameter values set in ITU-R P.681-7 for urban and dense urban scenarios to obtain the simulation results provided in Figs. 10 and 11; The modified parameter values are listed in Table II.

Fig. 7 shows the 10^3 local field measurements of pseudorange errors collected along a street in Daejeon, Korea (WGS-84 coordinates—Latitude: 36.3780526°; Longitude: 127.3934940°), where tall buildings of 30∼40 stories and small buildings of approximately five to ten stories appear in a mixed pattern. Fig. 7 also shows the sum of the distributions of the pseudorange errors obtained using the LMSC model (in ITU-R P.681-7) for environments with buildings of approximately an average number of stories for field buildings (in Table II, Building height [m]). The delays are calculated in

TABLE II
ITU-R P.681-7 CHANNEL MODELING PARAMETERS

Parameter	Value of Fig.7 (mean, std. dev., min., max.)	Value of Fig.8 (mean, std. dev. min., max.)
Carrier frequency [GHz]	1.5754	1.5754
Satellite elevation [Deg]	45	30 · 45 · 60
Satellite azimuth [Deg]	-45	-45
Vehicle heading [Deg]	0	0
Vehicle max. speed [km/h]	5	100
Vehicle and road center [m]	3	3
Road width [m]	24,-,-,-	24,-,-,-
Buildings and road center [m]	16,-,-,-	16,-,-,-
Building height [m]:		
Fig. 7 / Fig. 8(a)-El.30(1)	65,5,60,70	40,30,20,60
Fig. 8(a)-El.30(2)	-	60,30,40,80
Fig. 8(b)-El.45(1)	-	60,30,40,80
Fig. 8(b)-El.45(2)	-	80,30,60,100
Fig. 8(c)-El.60(1)	-	80,30,60,100
Fig. 8(c)-El.60(2)	-	100,30,80,120
Buiding Width [m]	30,10,20,-	30,10,20,-
Gap between buildings [m]	30,20,10,-	30,20,10,-
Likelihood of a gap	0.1	0.1
Tree height [m]	10,-,-,-	10,-,-,-
Tree diameter [m]	5,-,-,-	5,-,-,-
Tree trunk length [m]	2,-,-,-	2,-,-,-
Tree penetration loss [dB/m]	1.1,-,-,-	1.1,-,-,-
Distance: trees [m]	50,5,-,-	50,5,-,-
Distance: trees and road center[m]	14,1,-,-	14,1,-,-
Pole height [m]	5,-,-,-	5,-,-,-
Pole diameter [m]	0.5,-,-,-	0.5,-,-,-
Distance: poles [m]	40,10,-,-	40,10,-,-
Distance: poles and road center[m]	13,1,-,-	13,1,-,-

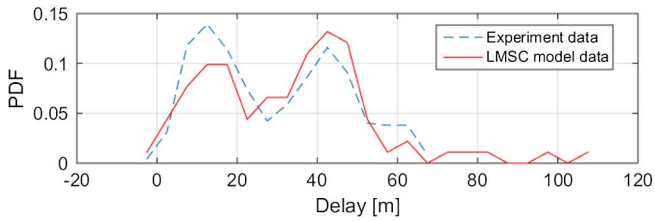

Fig. 7. Multipath delay distributions with field observation in an urban environment and with LMSC model simulations.

meters (i.e., [m]). As can be observed, there is a good agreement between the LMSC model and the field observations.

Fig. 8 shows the pseudorange error distributions obtained with the LMSC model; these results indicate that the NLOS delay distributions become wider and that their means increase as the satellite elevation angle decreases for the same environments, as represented in the legends of the figures. It is also shown that the LOS path occurs more often for satellites with a high elevation angle. In all simulation results obtained using the LMSC model, we find that $C/N_0 \leq 37$ dB-Hz for NLOS satellites, whereas $C/N_0 \geq 40$ dB-Hz for LOS satellites.

C. Performance of the Proposed Techniques

Here, we perform 10^3 Monte Carlo simulations with a cooperative vehicular network consisting of nine vehicles, traveling along an urban street and observing GNSS satellites, to demonstrate the performance of the proposed techniques MR-hcEKF and MRH-SPAWN. We compare the simulation results to those of the conventional hcEKF and H-SPAWN in terms of the RMS

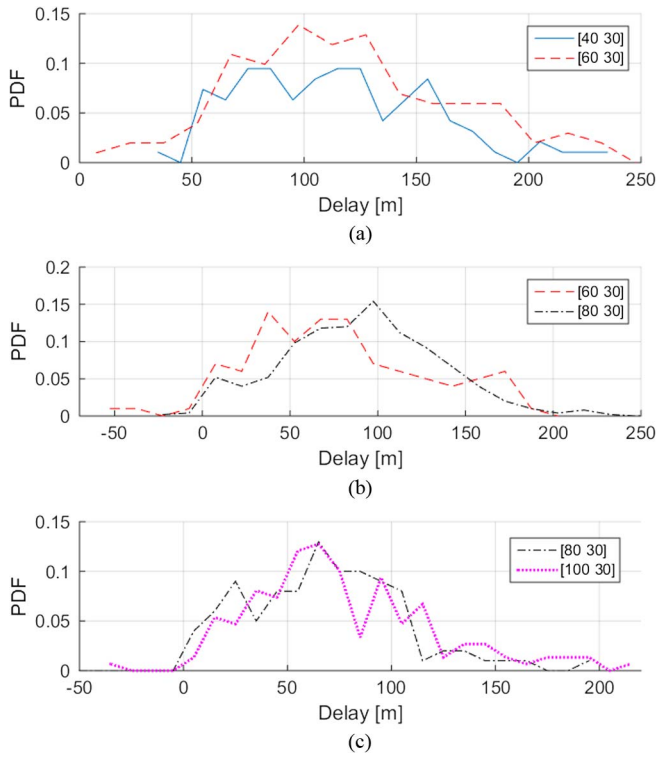

Fig. 8. Multipath delay distributions of the LMSC model data when the maximum vehicle speed is limited to 100 km/h in dense urban scenarios. The legends are [Mean of building heights, STD of building heights] in meters. (a) Satellite elevation is 30°. (b) Satellite elevation is 45°. (c) Satellite elevation is 60°.

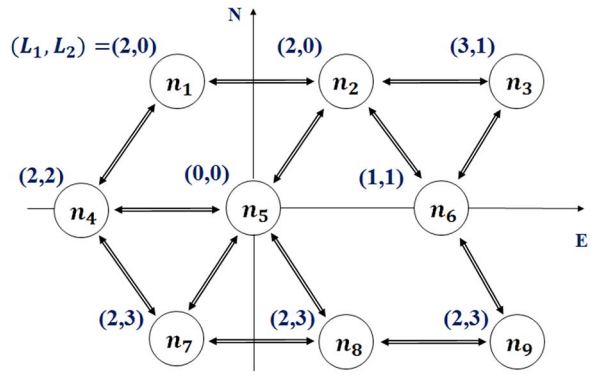

Fig. 9. Formation of the cooperative vehicular network and visible satellites for each vehicle (L_1, L_2).

error of the final position estimate in the xyz 3-D space. The conditions and assumptions for the Monte Carlo simulations are as follows.

- There are nine vehicles (n_m for $m = 1, 2, \ldots, 9$) on the road, represented by the circles shown in Fig. 9; their wireless connections are depicted as double-lined arrows. The numbers of LOS satellites and NLOS satellites are indicated in the upper left corner of each node. The relative locations of the vehicles are given in Table III.
- Vehicles are equipped with (D)GNSS receivers, and the observable GNSS satellites are uniformly distributed in the sky above an elevation angle of 30°.

TABLE III
VEHICLE RELATIVE LOCATIONS IN LOCAL ENU COORDINATE [M]

Vehicle	1	2	3	4	5	6	7	8	9
E	-10	10	30	-20	0	20	-10	10	30
N	17.3	17.3	17.3	0	0	0	-17.3	-17.3	-17.3
U	0	0	0	0	0	0	0	0	0

- The C/N_0's of the NLOS and LOS signals are uniformly distributed at [30, 40] dB-Hz and [40, 48] dB-Hz, respectively, and $\gamma_{C/N_0} = 42$ dB-Hz is used. In fact, we can use $\gamma_{C/N_0} > 42$ dB-Hz, which does not influence the result, as the nodes have at least two peer nodes in the simulations. The group ϕ_1 includes one LOS signal whose C/N_0 is less than 40 dB-Hz, which may represent an LOS signal attenuated by trees.
- Based on the empirical data, we use $\sigma_{v_{g,s_l \to u}} \simeq 7.5$ m for GNSS and $\sigma_{v_{d,s_l \to u}} \simeq 2.5$ m for DGNSS (there is a low variation depending on C/N_0) as in [2] and [31]. The local range noise $\sigma_{v_{n_l \to u}} = 1$ m [22], [23].
- The proposed technique runs for $K = 5$ time steps. At each time step k $(1 \leq k \leq K)$, new pseudorange and local range measurements are obtained. To determine the final position estimate, there are $I = 5$ iterations at each time step.
- At each iteration, we apply a parameter estimation algorithm based on importance sampling with 10^3 particles [15].
- We use $\gamma_t = 19$ m for GNSS and $\gamma_t = 7.5$ m for DGNSS to maintain a CFAR$\leq$1%.
- Based on the empirical data [24], where $\sigma_{\Delta_x^-} \leq 1$ m and $\sigma_{\Delta_y^-} \leq 1$ m, we use $\sigma_\Delta = 1$ m and $\sigma_b = 1$ m. Moreover, the predicted state uncertainty increases in four dimensions, i.e., $[x, y, z, t]$, at every time steps according to $[\sigma_\Delta^2, \sigma_\Delta^2, \sigma_\Delta^2, \sigma_b^2]$.

In the simulations, for every time steps k, each vehicle is given a new set of pseudorange measurements from a new set of satellites and a new set of local range measurements from the connected vehicles. The NLOS delays, received signal strength, and noise errors are independently generated at each k.

The positioning errors shown in Figs. 10 and 11 are the average of the final positioning errors after $K = 5$ time steps for each vehicles, determined using the CP techniques hcEKF, H-SPAWN, MR-hcEKF, and MRH-SPAWN. At each time step, the vehicles, due to their motion, are assumed at a new location. The techniques are given with new 3-D position and time prediction errors with uncertainties of $\sqrt{3}\sigma_\Delta (\simeq 1.72$ m) and $\sigma_b (= 1$ m), respectively.

The simulation results in Fig. 10 are based on the GNSS NLOS delays using the LMSC model (in ITU-R P.681-7) parameters, which produce pseudorange errors similar to those observed in the field shown in Fig. 7, in which most of the NLOS delays are less than 60 m. The results in Fig. 10(a) verify that the positioning performances of the conventional hcEKF and H-SPAWN techniques and of the proposed techniques are nearly identical for the vehicles n_1, n_2, and n_5, which do not use NLOS GNSS signals. However, the other six vehicles using the conventional hcEKF or H-SPAWN CP techniques

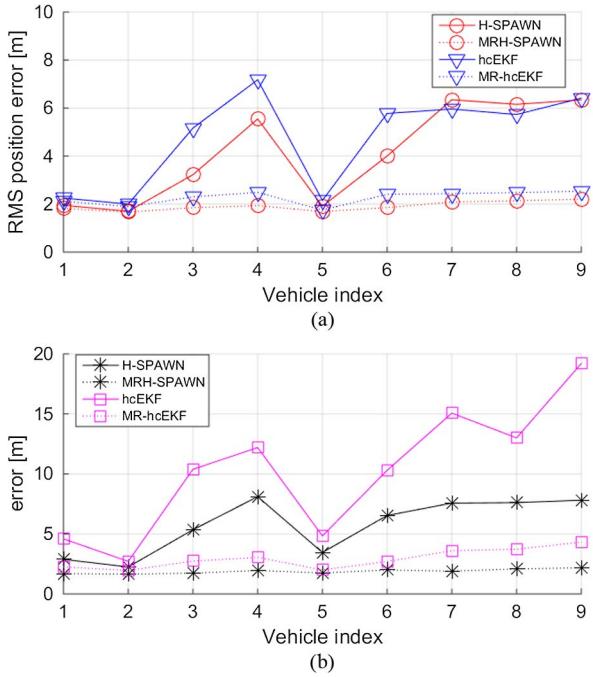

Fig. 10. Performance of the proposed techniques and conventional techniques for the NLOS delays shown in Fig. 7. (a) RMS position estimation errors for GNSS. (b) RMS position estimation errors for DGNSS.

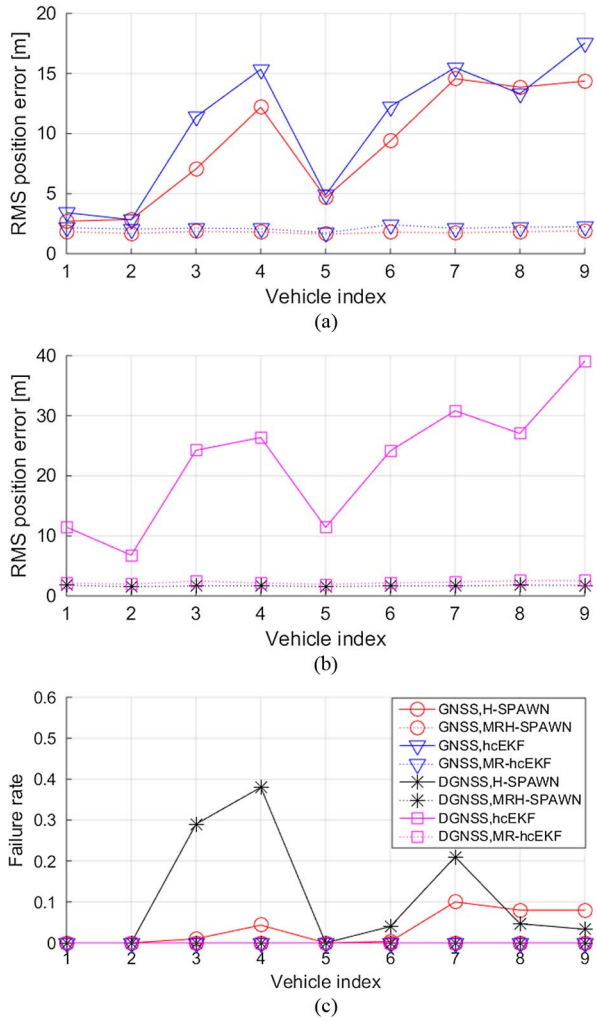

Fig. 11. Performance of the proposed techniques and conventional techniques for the LMSC model. (a) RMS position estimation errors for GNSS. (b) RMS position estimation errors for DGNSS. (c) Failure rate in GNSS and DGNSS.

suffer from NLOS GNSS, whereas the six vehicles using the proposed techniques do not experience performance degradation. In comparison to the results shown in Fig. 10(a), in which the vehicles are equipped with GNSS receivers and wireless ranging sensors, Fig. 10(b) shows results for vehicles equipped with DGNSS receivers and wireless ranging sensors. The position estimation performance shown in Fig. 10(b) is worse than that in Fig. 10(a), because the techniques have poor noise covariance (smaller DGNSS noise) for the same NLOS delays. The amounts of performance degradation with hcEKF and MR-hcEKF are larger than those with H-SPAWN and MRH-SPAWN, respectively, because hcEKF and MR-hcEKF are based on EKF, whereas H-SPAWN and MRH-SPAWN use the Bayesian inference in a near-optimal manner. The worst performance arises for vehicle n_9 because this vehicle has the largest number of NLOS GNSS signals and the lowest number of local ranging measurements.

The simulation results in Fig. 11 are based on GNSS NLOS delays using the LMSC model parameters, which produces the pseudorange errors observed in the field, as shown in Fig. 8, in which the NLOS delays range from 0 m to 150 m (or more). Similar to the results shown in Fig. 10(a) and (b), the simulation results in Fig. 11(a) and (b) are from vehicles equipped with wireless ranging devices and GNSS receivers and from vehicles with wireless ranging devices and DGNSS receivers, respectively. Because the NLOS delays shown in Fig. 8 are much larger than those shown in Fig. 7, the performance results for H-SPAWN and hcEKF shown in Fig. 11(a) are much worse than those in Fig. 10(a); the positioning errors of vehicles n_3, n_4, n_6, n_7, n_8, and n_9 can be seen to have nearly doubled. In comparison, the performance results for the proposed techniques MRH-SPAWN and MR-hcEKF show only slight differences. In addition, it is important to note that vehicles n_1, n_2, and n_5 have positioning errors larger than those shown in Fig. 10(a), which is not the case for the proposed techniques. The results in Fig. 11(a) confirm that the proposed techniques MRH-SPAWN and MR-hcEKF are only slightly affected by large NLOS delays, whereas the positioning errors of hcEKF are nearly doubled. In addition, H-SPAWN shows little robustness against large NLOS delays; H-SPAWN experiences positioning failure at least at one of the vehicles in the K sequential positioning, and the positioning failure propagates to all of the vehicles resulting in a cooperation failure as no single vehicle can determine its position alone. It should be noted that the positioning accuracy values shown in Fig. 11(a) and (b) are based only on successful CP. Fig. 11(b) shows that H-SPAWN fails when vehicles use DGNSS receivers. In fact, a positioning failure also occurs in the simulations shown in Fig. 11(a). This reveals that H-SPAWN is less robust against large NLOS delays than hcEKF. The failure rates for all vehicles are shown in Fig. 11(c); it can be seen that the high failure rate of H-SPAWN arises in vehicles using DGNSS receivers, compared with vehicles using GNSS. Other techniques were found to undergo

no failures during the 10^3 Monte Carlo simulations. Note that, as shown in Figs. 10 and 11, aspects of the positioning errors in the conventional techniques are related with the network topology. While vehicles n_1 and n_2 have two LOS and no NLOS satellite signals, n_2 has slightly smaller error than n_1. This is because n_2 utilizes two times more local range measurements than n_1. It can be also observed that, although n_2 and n_5 have very small positioning errors, n_2 has the smaller error than n_5 since n_2 receives two LOS satellite signals. On the contrary, the proposed techniques achieve almost the same positioning performance for all nine vehicles.

To test the performance of the proposed techniques for a general network topology, we perform 10^3 Monte Carlo simulations for a large-scale network with 21 vehicles in dynamic scenarios. The initial position of the 21 vehicles in three parallel lanes (seven vehicles with 20 m spacing per a lane) is set as

$$\mathbf{P}_{i,j}^{(0)} = \mathbf{P}_{i,1}^{(0)} + [20(j-1), 0, 0]^T \tag{49}$$

where $\mathbf{P}_{i,j}$ is the position for the j-th $(j \in \{1, 2, \ldots, 7\})$ vehicle in the i-th lane $(i \in \{1, 2, 3\})$ expressed in the ENU coordinate system, $(\cdot)^{(0)}$ represents the initial state, and the initial position of the leftmost vehicle in the i-th lane $\mathbf{P}_{i,1}$ is defined as $\mathbf{P}_{1,1} = [-10, 17.3, 0]^T$, $\mathbf{P}_{2,1} = [-20, 0, 0]^T$, and $\mathbf{P}_{3,1} = [-10, -17.3, 0]^T$ for the three lanes. We assume that the vehicles are moving west, and the velocity of the j-th vehicle in the i-th lane is expressed as

$$v_{i,j} = V_0 + \nu_i \left(\sin(2\pi f_i t) + \frac{1}{2} \sin(2\pi f_j t) \right) \tag{50}$$

where $V_0 = 60$ km/h is the mean traffic speed; $\nu_1 = 15$ km/h, $\nu_2 = 0$ km/h, and $\nu_3 = 30$ km/h are the mean relative velocities of the three lanes; f_i expresses the variation of the mean lane velocities ($f_1 = 0.1$ Hz, $f_2 = 0.05$ Hz, and $f_3 = 0.15$ Hz); and f_j is the relative speed variation of the j-th vehicle and follows a zero-mean Gaussian distribution with 1-Hz standard deviation. Therefore, the relative location of the vehicles is changing with time so that the network topology and the traffic densities are changing. At each time step k, each vehicle measures $\|U_n^{(k)}\|_0$ local ranges to $\|U_n^{(k)}\|_0$ nearest neighboring vehicles, and the number of observed LOS and NLOS GNSS satellites is $\|S_n^{(k)}\|_0$, where $\|U_n^{(k)}\|_0$ and $\|S_n^{(k)}\|_0$ are 2, 3, and 4 for (in average) 10, 7, and 4 vehicles, respectively, and the number of NLOS satellites is uniformly random in $[0, \|S_n^{(k)}\|_0]$. The average RMS position error of each vehicle is shown in Fig. 12; The conventional hcEKF and H-SPAWN have much larger error than MR-hcEKF and MRH-SPAWN, and similarly to the results shown in Fig. 11(b), H-SPAWN fails to deliver positioning fixes for DGNSS receivers. The results in Fig. 12 testify to the fact that the proposed techniques significantly outperform the conventional techniques in dynamic scenarios.

VI. Conclusion

In this paper, an ND algorithm has been proposed to enhance the multipath resistance of CP techniques. The proposed ND algorithm has shown strong NLOS detection performance and has been applied to two representative CP techniques: One is based on hcEKF, and the other is based on the hybrid SPA over wireless network (H-SPAWN). The theoretical expressions for the proposed CP techniques MR-hcEKF and MRH-SPAWN have been derived. Using numerous Monte Carlo simulations based on GNSS NLOS delays observed in practice, the performance of the proposed techniques has been compared with those of the hcEKF and H-SPAWN methods. It has been demonstrated that the proposed techniques strongly outperform hcEKF and H-SPAWN in both static and dynamic scenarios and are robust against multipath NLOS delays in urban environments.

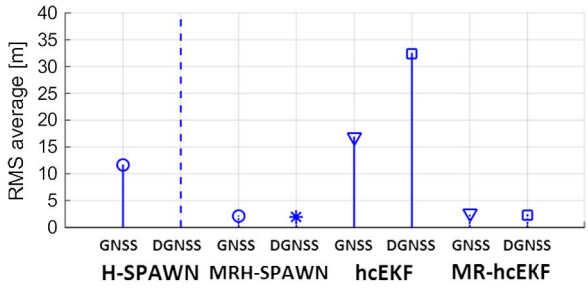

Fig. 12. Performance of the proposed techniques and conventional techniques in dynamic scenarios.

TABLE IV
Notation Summary

Notation	description
u, s, n	user, satellite, peer vehicle
s_l, n_l	l-th satellite, l-th peer vehicle
A $\rightarrow$ B	from A to B
$\mathbf{P}_i^{(k)}$	three-dimensional position state vector of $i(\in u, s, n)$ at time t_k
$\mathbf{x}, \hat{\mathbf{x}}^-, \hat{\mathbf{x}}$	true (1a), predicted (1b), estimated state vector (1c)
$\mathbf{\Sigma}_{\mathbf{x}_u}$	error covariance of the state $\mathbf{x}_u$
$d_{s\rightarrow u}^{(k)}$	true pseudorange (3a)
$\hat{d}_{s\rightarrow u}^{-(k)}$	predicted pseudorange (3b)
$\hat{d}_{s\rightarrow u}^{(k)}$	estimated pseudorange (3c)
ρ, $\boldsymbol{\rho}$	measured pseudorange (4), the set of ρ
$d_{n\rightarrow u}^{(k)}$	true local range (5a)
$\hat{d}_{n\rightarrow u}^{-(k)}$	predicted local range (5b)
$\hat{d}_{n\rightarrow u}^{(k)}$	estimated local range (5c)
r, $\boldsymbol{r}$	measured local range (6), the set of r
$v_{s\rightarrow u}$	pseudorange noise error (11)
$v_{d,s\rightarrow u}$	pseudorange noise error for DGNSS
$v_{g,s\rightarrow u}$	pseudorange noise error for GNSS
$v_{n\rightarrow u}$	local range noise error from peer vehicle to user
τ	NLOS delay [m]
$\boldsymbol{\zeta}$	range vector consists of $\boldsymbol{\rho}$ and $\boldsymbol{r}$
$\mathbf{\Lambda}$	diagonal predicted error covariance matrix with σ_Δ^2
$\mathbf{D}$	mean of $\boldsymbol{\zeta}$
$\mathbf{V}$	covariance of $\boldsymbol{\zeta}$
$\mathbf{\Sigma}_{\boldsymbol{\zeta}}$	diagonal measurement noise error covariance matrix (18)
ϕ_1	NLOS candidates in $\boldsymbol{\zeta}$
ϕ_2	LOS measurements in $\boldsymbol{\zeta}$
Z_{ϕ_1}	normalized detection variable (22)
Z_1	theoretical model of one-dimensional MD squares (48)
F_u	dynamics factor node; system dynamics (27b)
T_u^s	sat. factor node; pseudorange meas. likelihood (27c)
H_u^n	peer factor node; local range meas. likelihood (27d)
$\eta_{A\rightarrow B}$	message from A to B
w_l	weight factor for the l-th satellite (31)
γ_τ	NLOS delay detection threshold

Appendix

The summary of notations used in this paper are shown in Table IV.

REFERENCES

[1] G. Karagiannis *et al.*, "Vehicular networking: A survey and tutorial on requirements, architectures, challenges, standards and solutions," *IEEE Commun. Surveys Tuts.*, vol. 13, no. 4, pp. 584–616, 4th Quart. 2011.

[2] P. Misra and P. Enge, *Global Positioning System: Signals, Measurements, and Performance*, 2nd ed. Lincoln, MA, USA: Ganga-Jamuna, 2001.

[3] S.-H. Kong, "Analysis of code phase estimation error from resolved first arrival path," *IEEE Trans. Aerosp. Electron. Syst.*, vol. 50, no. 4, pp. 2456–2467, Oct. 2014.

[4] D. H. Titterton and J. L. Weston, *Strapdown Inertial Navigation Technology*, 2nd ed. London, U.K.: Inst. Eng. Technol., 2004.

[5] E. Uhlemann, "Introducing connected vehicles," *IEEE Veh. Technol. Mag.*, vol. 10, no. 1, pp. 23–31, Mar. 2015.

[6] N. Patwari *et al.*, "Locating the nodes: cooperative localization in wireless sensor networks," *IEEE Signal Process. Mag.*, vol. 22, no. 4, pp. 54–69, Jul. 2005.

[7] S. Gezici *et al.*, "Localization via ultra-wideband radios: A look at positioning aspects for future sensor networks," *IEEE Signal Process. Mag.*, vol. 22, no. 4, pp. 70–84, Jul. 2005.

[8] N. Alam, A. T. Balaei, and A. G. Dempster, "A DSRC doppler-based cooperative positioning enhancement for vehicular networks with GPS availability," *IEEE Trans. Veh. Technol.*, vol. 60, no. 9, pp. 4462–4470, Nov. 2011.

[9] A. H. Rabiain, A. Kealy, and M. Morelande, "Improving the low cost INS/GNSS solution using cooperative positioning and robust dynamic modelling techniques," in *Proc. IGNSS Symp.*, Gold Coast, Qld., Australia, Jul. 2013, pp. 1–15.

[10] M. A. Caceres, F. Sottile, R. Garello, and M. A. Spirito, "Hybrid GNSS-ToA localization and tracking via cooperative unscented Kalman filter," in *Proc. IEEE 21st Int. Symp. PIMRC*, Istanbul, Turkey, Sep. 2010, pp. 271–275.

[11] L. C. Bento, R. Parafita, and U. Nunes, "Inter-vehicle sensor fusion for accurate vehicle localization supported by V2V and V2I communications," in *Proc. IEEE 15th Int. Intell. Transp. Syst. Conf.*, Anchorage, AK, USA, Sep. 2012, pp. 907–914.

[12] F. Sottile, H. Wymeersch, M. A. Caceres, and M. A. Spirito, "Hybrid GNSS-terrestrial cooperative positioning based on particle filter," in *Proc. IEEE GLOBECOM*, Houston, TX, USA, 2011, pp. 1–5.

[13] H. Wymeersch, J. Lien, and M. Z. Win, "Cooperative localization in wireless networks," *Proc. IEEE*, vol. 97, no. 2, pp. 427–450, Feb. 2009.

[14] F. R. Kschischang, B. J. Frey, and H. A. Loeliger, "Factor graphs and the sum–product algorithm," *IEEE Trans. Inf. Theory*, vol. 47, no. 2, pp. 498–519, Feb. 2001.

[15] M. A. Caceres, F. Penna, H. Wymeersch, and R. Garello, "Hybrid cooperative positioning based on distributed belief propagation," *IEEE J. Sel. Areas Commun.*, vol. 29, no. 10, pp. 1948–1958, Dec. 2011.

[16] W. Nam and S. H. Kong, "Least-square-based iterative multipath superresolution techniques," *IEEE Trans. Signal Process.*, vol. 61, no. 3, pp. 519–529, Feb. 2013.

[17] J. K. Ray, M. E. Cannon, and P. Fenton, "GPS code and carrier multipath mitigation using a multiantenna system," *IEEE Trans. Aerosp. Electron. Syst.*, vol. 37, no. 1, pp. 183–195, Jan. 2001.

[18] J. Meguro, T. Murata, J. Takiguchi, Y. Amano, and T. Hashizume, "GPS multipath mitigation for urban area using omnidirectional infrared camera," *IEEE Trans. Intell. Transp. Syst.*, vol. 10, no. 1, pp. 22–30, Mar. 2009.

[19] S. Feng, W. Y. Ochieng, D. Walsh, and R. Ioannides, "A measurement domain receiver autonomous integrity monitoring algorithm," *GPS Solut.*, vol. 10, no. 2, pp. 85–96, May 2006.

[20] N. L. Knight and J. Wang, "A comparison of outlier detection procedures and robust estimation methods in GPS positioning," *J. Navigat.*, vol. 62, no. 4, pp. 699–709, 2009.

[21] T. Binjammaz, A. Al-Bayatti, and A. Al-Hargan, "GPS integrity monitoring for an intelligent transport system," in *Proc. IEEE Position. Navigat. Commun. Conf.*, Dresden, Germany, Mar. 2013, pp. 1–6.

[22] C. C. Chong, F. Watanabe, and M. Z. Win, "Effect of bandwidth on UWB ranging error," in *Proc. IEEE WCNC*, Kowloon, Hong Kong, China, Mar. 2007, pp. 1559–1564.

[23] V. Kristem, A. F. Molisch, S. Niranjayan, and S. Sangodoyin, "Coherent UWB ranging in the presence of multiuser interference," *IEEE Trans. Wireless Commun.*, vol. 13, no. 8, pp. 4424–4439, Aug. 2014.

[24] R. Schubert *et al.*, "Empirical evaluation of vehicular models for ego motion estimation," in *Proc. IEEE Intell. Veh. Symp.*, Baden-Baden, Germany, Jun. 2011, pp. 534–539.

[25] J. T. Isaacs, A. T. Irish, F. Quitin, U. Madhow, and J. P. Hespanha, "Bayesian localization and mapping using GNSS SNR measurements," in *Proc. PLANS*, Monterey, CA, USA, May 2014, pp. 445–451.

[26] A. Papoulis, *Probability, Random Variables, and Stochastic Processes*, 3rd ed. New York, NY, USA: McGraw-Hill, 1991.

[27] P. Mahalanobis, "On the generalized distance in statistics," in *Proc. Nat. Inst. Sci. India*, Calcutta, India, 1936, vol. 12, pp. 49–55.

[28] I. C. F. Ipsen and D. J. Lee, "Determinant approximations," *Numer. Linear Algebra Appl.* [Online]. Available: http://arxiv.org/abs/1105.0437

[29] D. Simon, *Optial State Estimation: Kalman, H_∞, and Nonlinear Approaches*. Hoboken, NJ, USA: Wiley, 2006.

[30] S. Särkkä, *Bayesian Filtering and Smoothing*. New York, NY, USA: Cambridge Univ. Press, 2013.

[31] P. K. Enge, R. M. Kalafus, and M. F. Ruane, "Differential operation of the global positioning system," *IEEE Commun. Mag.*, vol. 26, no. 7, pp. 48–60, Jul. 1988.

[32] G. J. Myatt, *Making Sense of Data: A Practical Guide to Exploratory Data Analysis and Data Mining*. New York, NY, USA: Wiley-Interscience, 2006.

[33] "Propagation Data Required for the Design of Earth-Space Land Mobile Telecommunication Systems," Int. Telecommun. Union (ITU), Geneva, Switzerland, Recommendation ITU-R P.681-7, Oct. 2009.

Hyunwoo Ko received the B.S. degree from Handong Global University, Pohang, Korea, in 2014.

Since 2014, he has been working toward the Master's degree with CCS Graduate School for Green Transportation, Korea Advanced Institute of Science and Technology, Daejeon, Korea. His research interests include autonomous navigation systems, sensor fusion, and positioning technologies.

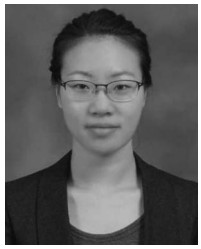

Binhee Kim (S'08) received the B.S.E.E. and M.S.E.E. degrees from the Korea Advanced Institute of Science and Technology (KAIST), Daejeon, Korea, in 2008 and 2010, respectively. She is currently working toward the Ph.D. degree with CCS Graduate School for Green Transportation, KAIST.

Her research interests include super-resolution signal processing, detection, and estimation for navigation systems.

Seung-Hyun Kong (M'06) received the B.S. degree in electronics engineering from Sogang University, Seoul, Korea, in 1992; the M.S. degree in electrical engineering from NYU Polytechnic School of Engineering, New York, NY, USA, in 1994; and the Ph.D. degree in aeronautics and astronautics from Stanford University, Stanford, CA, USA, in 2006.

From 1997 to 2004, he was with Samsung Electronics Inc. and Nexpilot Inc., both in Korea, where his research focused on wireless communication systems and Universal Mobile Telecommunications Service mobile positioning technologies. In 2006 and from 2007 to 2009, he was a staff engineer with Polaris Wireless Inc., Santa Clara, CA, and with Corporate R&D Center, Qualcomm Inc., San Diego, CA, respectively, where his research was on assisted Global Navigation Satellite Systems (GNSS) and wireless positioning technologies such as wireless location signature and mobile-to-mobile positioning technologies. Since 2010, he has been with the Korea Advanced Institute of Science and Technology, Daejeon, Korea, where he is currently an Associate Professor with CCS Graduate School for Green Transportation. His research interests include next-generation GNSS, advanced signal processing for navigation systems, and vehicular communication systems.